Article

SOURCE DATA | TRANSPARENT PROCESS | OPEN ACCESS | CHECK FOR UPDATES

EMBO reports

Evolution of intrinsically disordered regions in vertebrate galectins for phase separation

Yu-Hao Lin [1,2,5], Yu-Chen Chen[1,5], Yung-Chen Sun[1,2] & Jie-rong Huang [1,3,4]✉

Abstract

Intrinsically disordered regions (IDRs) are widespread in proteins, yet their evolutionary paths remain poorly understood. Using galectin, a universal carbohydrate-binding protein, we investigated how IDRs evolved and acquired their biological roles in vertebrates. Through extensive proteome-wide sequence analyses, we found that vertebrate galectin IDRs share overall amino acid compositions but differ significantly in their aromatic residue types. Using nuclear magnetic resonance (NMR) spectroscopy and lipopolysaccharide micelle assays, we demonstrated that despite these differences, IDRs from various vertebrate galectins independently converged toward a similar function: mediating agglutination via phase separation. Our data suggest that the specific types of aromatic residues within these IDRs were established early in evolution and underwent independent expansions among different vertebrate lineages. Additionally, we identified a conserved short N-terminal motif critical for promoting galectin self-association, which likely served as an incipient sequence for subsequent IDR evolution. Contrary to previous peptide studies emphasizing aromatic residue specificity, our findings highlight the evolutionary preference for increasing motif repetition over residue-type optimization to achieve functional fitness.

Keywords Liquid-Liquid Phase Separation; Intrinsically Disordered Proteins; Protein Evolution; NMR; Galectin
Subject Categories Evolution & Ecology; Structural Biology
https://doi.org/10.1038/s44319-026-00692-w
Received 23 June 2025; Revised 16 December 2025; Accepted 12 January 2026
Published online: 02 February 2026

Introduction

Proteins' functions are determined by their unique shapes, encoded in their amino acid sequences. The sequences have been shaped by natural selection to adapt new functions or optimize existing ones, varying through evolution (Jayaraman et al, 2022). Regardless of the sequence diversity, conserved patterns hint at the existence of common ancestors (Capra and Singh, 2007), and levels of similarity between protein sequences reveal phylogenetic relationships and evolutionary routes (Zuckerkandl and Pauling, 1965). Protein evolutionary paths also provide information to predict tertiary structures from their sequences as exploited in classical homology modeling (Waterhouse et al, 2018) and in recent machine learning approaches (Jumper et al, 2021). However, intrinsically disordered proteins (IDPs) or proteins with intrinsically disordered regions (IDRs) exhibit limited homolog sequence similarity and are structurally unpredictable (Akdel et al, 2022), making their emergence evolutionarily intriguing.

At least half of the eukaryotic proteins have IDRs (Dunker et al, 2000). Their functions include increasing binding surface areas, facilitating post-translational modifications, serving as versatile hubs for interactions with multiple partners, and acting as linkers in multiple folded domains (Holehouse and Kragelund, 2024). Another key characteristic of proteins with IDRs is their ability to phase separate (PS), which is the main mechanism of membraneless organelle (biomolecular condensate) formation for the spatiotemporal control in many biological functions (Banani et al, 2017; Shin and Brangwynne, 2017). The "spacer" and multivalent "sticker" motifs borne by the IDRs in these proteins, respectively, provide the flexibility and adhesive properties required to drive PS (Harmon et al, 2017; Holehouse and Pappu, 2018). However, without structural constraints, the evolutionary paths to these various functions remain unclear and challenging to study.

IDRs may have coevolved with folded partners by enhancing affinities at binding interfaces (Jemth et al, 2018; Karlsson et al, 2022; Mihalic et al, 2024). The length of linker IDRs connecting structural domains is also adaptable to optimize the binding affinity (Gonzalez-Foutel et al, 2022). In our previous work on a paralog protein family, we demonstrated that different physicochemical properties can converge to the same function (Chiu et al, 2022). Using ortholog databases, we also demonstrated that aromatic residues are more likely to appear in the IDRs of RNA-binding proteins to promote PS (e.g., in stress granules) (Ho and Huang 2022). Furthermore, selective pressures seem to preserve PS propensity in certain IDR-rich proteins, such as the FET protein family (Dasmeh et al, 2021; Dasmeh and Wagner, 2021) and DEAD-box ATPases (Hondele et al, 2019). Protein ortholog databases also provide valuable training datasets for machine learning to detect IDR features (Lu et al, 2022; Ho et al, 2023). However, these databases are mainly based on sequence or

[1]Institute of Biochemistry and Molecular Biology, National Yang Ming Chiao Tung University, No. 155 Section 2 Li-nong Street, Taipei, Taiwan. [2]Taiwan International Graduate Program in Molecular Medicine, National Yang Ming Chiao Tung University and Academia Sinica, Taipei, Taiwan. [3]Department of Life Sciences and Institute of Genome Sciences, National Yang Ming Chiao Tung University, No. 155 Section 2 Li-nong Street, Taipei, Taiwan. [4]Institute of Biomedical Informatics, National Yang Ming Chiao Tung University, No. 155 Section 2 Li-nong Street, Taipei, Taiwan. [5]These authors contributed equally: Yu-Hao Lin, Yu-Chen Chen. ✉E-mail: jierongh@nycu.edu.tw

functional similarities in folded domains, and the evolution routes of IDRs remain relatively less explored.

Here, we address this issue by examining galectin-3, a β-galactoside-binding lectin featuring a folded carbohydrate-recognition domain (CRD) and an intrinsically disordered N-terminal domain (NTD). In our previous biophysical and structural studies, we showed that NTDs self-associate and make fuzzy contacts with the CRD's non-carbohydrate-binding site (hereafter, the NTD-binding face) in both intra- and intermolecular modes (Fig. EV1) (Lin et al, 2017). These interactions drive galectin-3 phase separation via π–π interactions and explain that the protein's agglutination arises not from dimeric or tandem CRD repeats but from multivalent NTD-mediated association (Fig. EV1) (Chiu et al, 2020). We further assessed cation-π interactions contributed by conserved, positively charged residues at the NTD-binding face (Fig. EV1) (Sun et al, 2024). This detailed mechanistic framework makes galectin-3 a suitable model for our analysis. In this work, using proteome-wide sequence analysis, biophysical assays, and nuclear magnetic resonance (NMR) spectroscopy, we found that IDR-tethered galectins are widespread across diverse taxa, including most animals. In vertebrates, although galectin IDR sequences are similar in composition, they differ in the types of aromatic residues and their flanking motifs. Our results indicate that the agglutination capacity of these aromatic residues depends primarily on the number rather than the specific type of aromatic sequence motifs in the IDRs. This finding underscores the adaptability of these proteins and provides insights into the intriguing evolutionary trajectories of IDRs.

Results

Proteome-wide analysis of aromatic-containing motifs in galectins with intrinsically disordered regions

In the orthologous matrix (OMA) database (Altenhoff et al, 2021), ~100 proteins are annotated as orthologous to human galectin-3 (hGal3, OMA group number: 1215955). As expected, their amino acid compositions and sequence-predicted levels of the structural disorder are similar (Dataset EV1). However, to investigate how widespread IDR-bearing galectins are in the entire proteome, we searched for homologs using only the human CRD sequence. We used the BLAST algorithm (Zaru et al, 2023) to query the TrEMBL database (UniProt, 2023) (~200 million sequences) on a local computer with an *E*-value criterion of 0.1. This search returned ~17,000 proteins with at least 21% sequence identity to the CRD of hGal3. Among these, 1321 proteins contain at least 75 consecutive residues predicted to be disordered (disorder score >0.5) by IUPRED3 (Erdos et al, 2021) (Fig. 1A). Dataset EV2 shows the predicted disordered regions, amino acid composition, and the phylogenetic relations of these 1321 protein sequences. Representative examples from each phylum are depicted in Fig. 1B. Notably, the amino acid compositions of these IDRs differ among phyla and exhibit little sequence conservation, suggesting that IDRs tethered to galectin CRDs likely arose independently in different lineages (also see Discussion). For instance, IDRs in nematodes (e.g., *C. elegans*) and arthropods (e.g., *Drosophila*) contain higher proportions of negatively charged amino acids (aspartate and glutamate), whereas chordate IDRs (including those in vertebrates) are enriched in proline, glycine, and alanine (Fig. 1B).

This similarity of amino acid patterns among vertebrates is in keeping with previous observations in model organisms (Chiu et al, 2020), whereby we found that the functional role of the aromatic residues in hGal3's IDR is to drive agglutination (Chiu et al, 2020). Although the IDRs have similar compositions, the types of aromatic residues present differ between vertebrates (Fig. 1C shows the distributions of %W, %F, and %Y in IDRs across vertebrates, alongside representative pie charts from Dataset EV3). For instance, aromatic residue compositions are more variable in fish galectins' IDRs than in those of amphibians, while tyrosine predominates in mammals. Of the 1321 sequences with predicted IDRs longer than 75 amino acids, 351 of them share an IDR amino acid composition analogous to hGal3, namely >8% aromatic residues (phenylalanine, F; tyrosine, Y; tryptophan W) and <3% negatively charged residues (D, E; Fig. 1A), a subset manageable for motif searches using the MEME suite web server (Bailey et al, 2015). Detailed information on their predicted disorder, amino acid compositions of these IDRs, and phylogenetic trees is available in Dataset EV3). The MEME results for all sequences are shown in Fig. 1D in a compact format for an overview. An accompanying HTML file in Dataset EV4 provides interactive features for more detailed motif information. For visual clarity, ~20 representative sequences spanning different taxonomic groups were selected (Fig. 1E; Appendix Fig. S1A). Comparing sequence motifs revealed many similarities in the CRD between species, as expected (Fig. 1D,E; same color blocks between different species, identified by BLAST). Notably, many motifs also occur multiple times within the same IDR (Fig. 1D,E; same color blocks within each sequence), several of which are shown in Fig. 1F. Furthermore, all the analyzed sequences have similar motifs at the N-terminus (Fig. 1D,E), and three of which are mapped onto residues 5–20 of hGal3 in Fig. 1G. From the motif patterns (Fig. 1E), we sought to understand whether the repeats in galectin IDRs share a common ancestral origin or if they emerged through multiple duplications of a shorter motif (Fig. 1H). The IDR-tethered galectin in zebrafish (zfGal) is particularly interesting because of the predominance of tryptophan-based motifs, in contrast to the tyrosine-based motifs in hGal3 (Fig. 1I; Appendix Fig. S1B). The respective predominance of tryptophan and tyrosine does not reflect a difference in the distribution of amino acids in the corresponding proteomes (Appendix Fig. S1C). Consequently, we selected this zebrafish galectin as a model system to experimentally investigate the effects of particular aromatic amino acids and explore possible evolutionary routes.

Zebrafish galectin agglutination

Zebrafish galectin has similar structural disorder and prion-likeness scores to those of hGal3 (Fig. 2A), and the AlphaFold-predicted structure of the CRD is similar to the experimentally determined structure of hGal3's CRD (PDB code: 2NMO; Fig. 2B). Furthermore, circular dichroism (CD) spectra analysis of zfGal (purified from bacteria with synthetic cDNA) showed similar secondary structure populations as in hGal3 (Fig. 2C,D).

One of hGal3's functions is to agglutinate glycosylated molecules through PS via its IDR (Chiu et al, 2020). Comparable predicted levels of π-π interactions and PS propensities in zfGal and hGal3 suggest their similar condensation ability (Fig. 2E). Zebrafish galectin agglutination was experimentally investigated using lipopolysaccharide (LPS) micelle

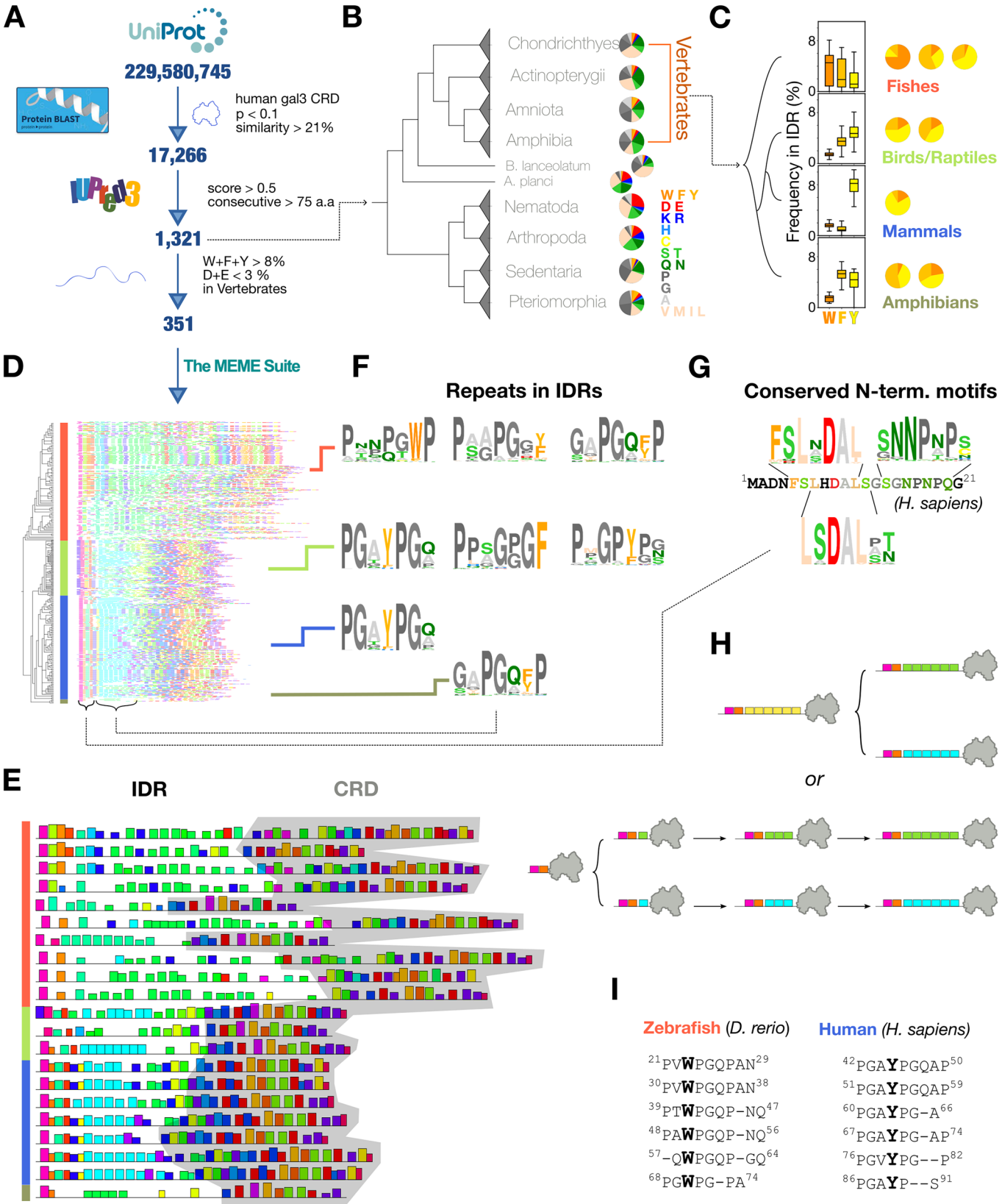
A
UniProt
229,580,745
Protein BLAST
human gal3 CRD
p < 0.1
similarity > 21%
17,266
IUPred3
score > 0.5
consecutive > 75 a.a
1,321
W+F+Y > 8%
D+E < 3 %
in Vertebrates
351
The MEME Suite
B
Chondrichthyes
Actinopterygii
Amniota
Amphibia
Vertebrates
B. lanceolatum
A. planci
Nematoda
Arthropoda
Sedentaria
Pteriomorphia
C
Frequency in IDR (%)
Fishes
Birds/Raptiles
Mammals
Amphibians
D
F
Repeats in IDRs
G
Conserved N-term. motifs
1MADNFSLHDALSGSGNPNPQG21
(H. sapiens)
H
or
E
IDR
CRD
I
Zebrafish (D. rerio)
Human (H. sapiens)
21PVWPGQPAN29
30PVWPGQPAN38
39PTWPGQP-NQ47
48PAWPGQP-NQ56
57-QWPGQP-GQ64
68PGWPG-PA74
42PGAYPGQAP50
51PGAYPGQAP59
60PGAYPG-A66
67PGAYPG-AP74
76PGVYPG--P82
86PGAYP--S91

Figure 1. Sequence analysis of galectins with long (>75 amino acids) intrinsically disordered regions (IDRs).

(**A**) Flowchart of the analysis with algorithms and selection criteria. (**B**) Taxonomical grouping of galectins with IDRs longer than 75 amino acids. Representative amino acid distributions are shown as pie charts. (**C**) Boxplots show the distributions of W, F, and Y content (percent of IDR) in galectin homologs across major vertebrate clades (median and interquartile range shown; whiskers denote 1.5 × IQR). Representative pie charts further illustrate the aromatic composition per group (W: tryptophan, F: phenylalanine, Y: tyrosine; all data in Dataset EV3). (**D**) Sequence motifs identified by the MEME suite (Bailey et al, 2015). The color blocks in each sequence represent frequently appearing motifs (see Dataset EV4 for additional information). (**E**) Representative MEME results selected from panel *D*. The carbohydrate-recognition domain (CRD) is shaded gray. (**F**) Representative repeated motifs in IDRs. (**G**) N-terminal conserved sequences aligned with human galectin-3. (**H**) Schematic illustration of possible evolutionary models. (**I**) Aligned repeated sequences in zebrafish (*Danio rerio*) and human galectin IDRs. Source data are available online for this figure.

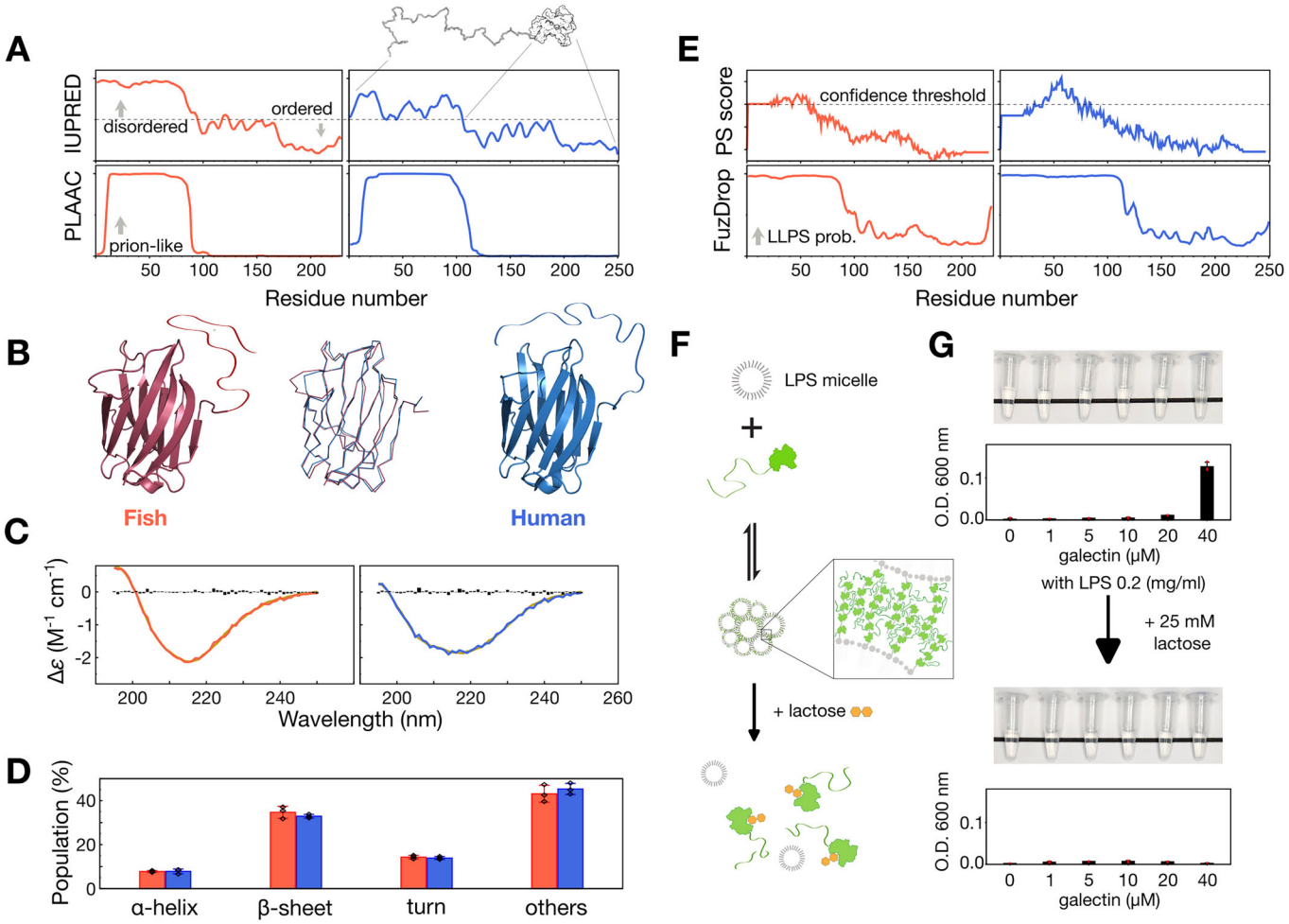

Figure 2. Sequence and structural analysis of the IDR-tethered galectin in zebrafish.

(**A**) Levels of protein disorder and prion-likeness predicted respectively by IUPRED (Erdos et al, 2021) and PLAAC (Lancaster et al, 2014). (**B**) AlphaFold (Jumper et al, 2021) structural model of zebrafish galectin (left), experimentally determined structure of human galectin-3 (PDB: 2NMO; right), and best alignment of the two structures (middle). (**C**) Circular dichroism (CD) spectra of IDR-tethered zebrafish galectin and human galectin-3 (experimental data in red (zebrafish) or blue (human), best-fit curves from the BeStSel web server (Micsonai et al, 2015; Micsonai et al, 2018) in gray, and residuals as black bars). (**D**) Comparison of secondary structure components derived from BeStSel fitting. (**E**) Predicted phase separation propensities using PS score (Vernon et al, 2018) and FuzDrop web server (Hardenberg et al, 2020). (**F**) Schematic illustration of using lipopolysaccharide (LPS) micelles to test the agglutination capacity of galectins and their reversibility. (**G**) Photographs and corresponding optical density measurements at 600 nm of differently concentrated samples of zebrafish galectin mixed with 0.2 mg/ml LPS micelles (top) and after adding 25 mM lactose (bottom). (CD and optical density measurements were performed in triplicate and results are reported as mean ± s.d.). Source data are available online for this figure.

assays, based on our previous findings that LPS micelles are agglutinated by hGal3 and that the condensates can be reversed to monomers by adding lactose (a galectin-3's ligand that blocks interactions between the sugar moiety of the LPS micelles and the CRD, Fig. 2F) (Chiu et al, 2020). The fact that zebrafish galectin samples were turbid in the presence of LPS but became transparent again when lactose was added (Fig. 2G) suggests therefore that the IDR in zfGal drives agglutination as it in hGal3.

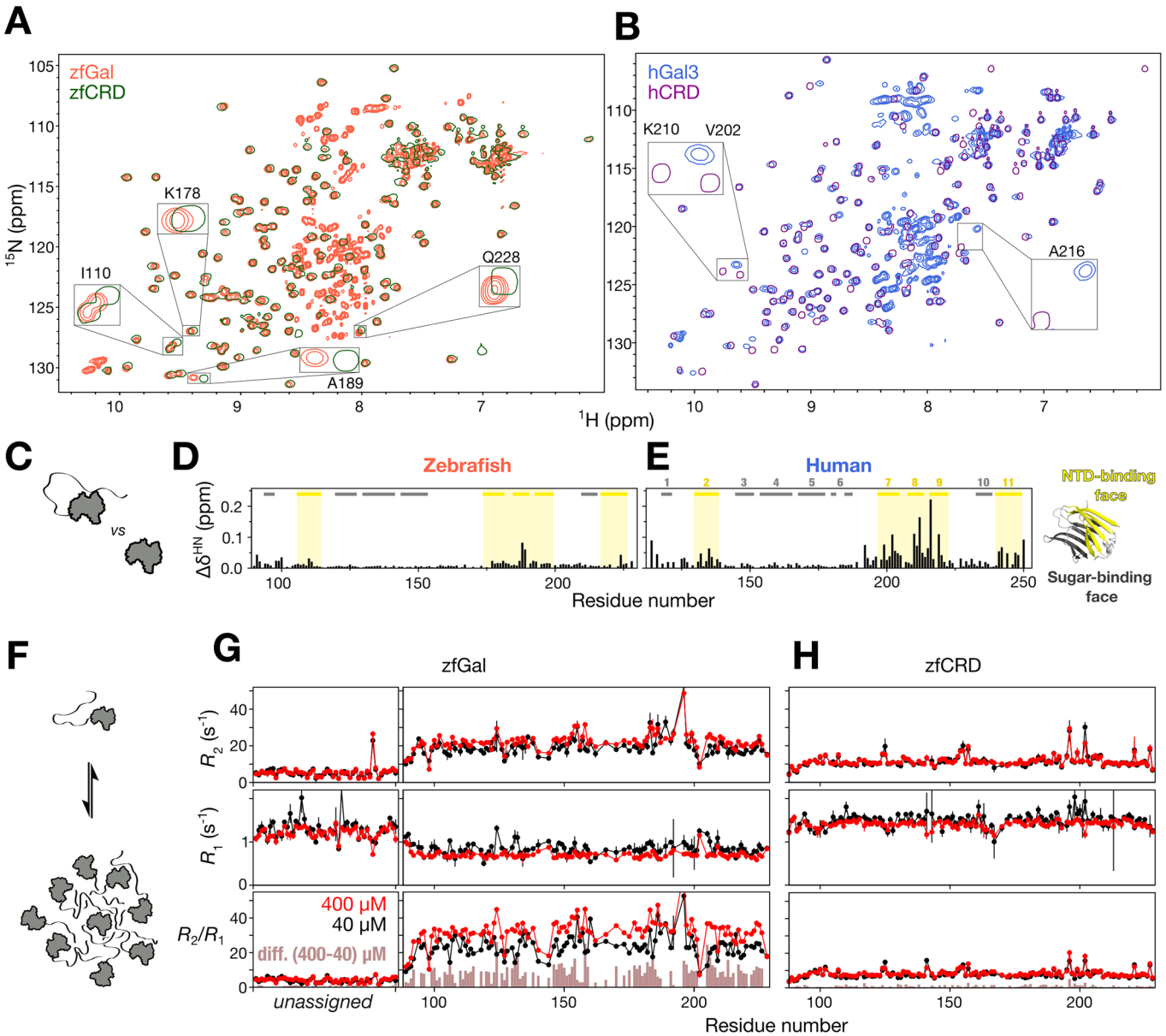

Figure 3. Inter- and intramolecular interactions in zebrafish IDR-tethered galectin.

(**A**, **B**) Overlaid HSQC spectra of full-length and carbohydrate-recognition domain (CRD)-only constructs of (**A**) zebrafish (full-length, orange; CRD-only, green) IDR-tethered galectin and (**B**) human (full-length, blue; CRD-only, purple) galectin-3. (**C–E**) Average chemical shift perturbations in the presence of the IDR for (**D**) zebrafish galectin and (**E**) human galectin-3 derived from the spectra shown in panels (**A**, **B**). Residues on the N-terminal domain binding side of the CRD are highlighted in yellow. (**F–H**) Transverse (R_2) and longitudinal (R_1) relaxation rate constants and R_2/R_1 ratio as a function of residue number (residues in the intrinsically disordered N-terminal domain are unassigned) measured in 400 µM (red) and 40 µM (black) samples of (**G**) full-length zebrafish galectin and (**H**) its CRD-only construct. Error bars indicate ±1 standard deviation (1σ) of the fitted R_1 and R_2 values estimated by Monte Carlo analysis (see Methods). The brown bars are the difference in R_2/R_1 ratios between high and low concentrations. Source data are available online for this figure.

Similar inter- and intramolecular IDR–CRD interactions in human and zebrafish galectin

Human galectin-3 agglutinates via fuzzy inter- and intramolecular interactions between the intrinsically disordered NTD and CRD (Lin et al, 2017), which manifest in NMR chemical shift perturbations and relaxation rate changes. Although the CRD structures of zfGal and hGal3 are similar, their ^{1}H-^{15}N heteronuclear single-quantum coherence (HSQC) spectra are noticeably different (Fig. 3A,B; Appendix Fig. S2A,B). We thus assigned the chemical shifts of zfGal without the IDR (residues 1–83 removed, zfCRD; note that the IDR chemical shifts are uninformative for this analysis, which focuses on CRD sites that the IDR interacts with; Appendix Fig. S2C). The largest changes in peak positions between the CRD-only constructs and the full-length proteins are clustered in the non-carbohydrate-binding face,

Table 1. NMR dynamic analysis of zfGal protein constructs.

Construct	zfGal		zfCRD		zfGal$^{W/Y}$	
Conc. (μM)	40	400	40	400	40	400
R_2	17.03 ± 0.29	21.05 ± 0.31	10.05 ± 0.14	10.97 ± 0.17	18.83 ± 0.36	22.73 ± 0.49
$\|\Delta R_2\|$	4.03 ± 0.43		0.92 ± 0.22		3.90 ± 0.61	
R_1	0.82 ± 0.01	0.72 ± 0.01	1.48 ± 0.01	1.41 ± 0.01	0.76 ± 0.01	0.65 ± 0.01
$\|\Delta R_1\|$	0.10 ± 0.01		0.07 ± 0.01		0.10 ± 0.01	
R_2/R_1	20.65 ± 0.46	29.26 ± 0.54	6.79 ± 0.10	7.75 ± 0.13	24.90 ± 0.53	34.87 ± 0.84
$\|\Delta(R_2/R_1)\|$	8.61 ± 0.71		0.96 ± 0.16		9.97 ± 1.00	

Dynamic analysis for the indicated constructs corresponding to Figs. 3G (zfGal), F (zfCRD) and 4F (zfGalW/Y). Only residues in the carbohydrate-recognition domain (CRD) were analyzed. For each condition (40 and 400 μM), R_2 and R_1 are inverse-variance weighted (IVW) means of the residue-wise estimates; standard errors (SEs) are the IVW SEs. ΔR_2 and ΔR_1 are the direct differences of the condition means. R_2/R_1 is the ratio of the IVW means at the same concentration, and $\Delta(R_2/R_1)$ is the difference between concentrations. Uncertainties for R_2/R_1, ΔR_2, ΔR_1, and $\Delta(R_2/R_1)$ are obtained by standard error propagation from the reported SEs of the IVW means.

indicating that these changes are due to the presence/absence of IDR interactions with the CRD (Fig. 3C,D). These chemical shift perturbations are less pronounced in zfGal (Fig. 3D) than they are in hGal3 (Fig. 3E).

To probe self-association, we compared concentration-dependent NMR spectra and dynamics to shift the monomer-oligomer equilibrium. Our earlier work showed that intermolecular interactions are negligible at 40 μM, whereas self-association is markedly increased at 400 μM without entering the PS regime (Lin et al, 2017). Consistent with this, the NMR spectra of zfGal at high (400 μM) and low (40 μM) concentrations overlap closely but the peak intensity ratios differ from the molar ratio (Appendix Fig. S3), most likely because of self-association (Fig. 3F). In NMR spin relaxation experiments, R_2 rates were higher and R_1 rates lower in the higher concentration sample (Fig. 3F,G; Table 1), which is typical of a shift in the equilibrium toward a bound (in this case self-associated) conformation (Fushman et al, 1997; Pfuhl et al, 1999; Korchuganov et al, 2001; Akerud et al, 2002; Baryshnikova and Sykes, 2006; Jensen et al, 2008). No such concentration-related differences were observed in the CRD-only construct (Fig. 3H; Table 1), indicating that this self-association is mediated by the intrinsically disordered NTD. Overall, therefore, these results suggest that intra- and intermolecular interactions in zfGal and hGal3 are similar but less pronounced in the former than in the latter.

Effects of aromatic residue type on self-association and agglutination

To investigate the extent to which self-association and agglutination depend on the particular type of aromatic residue in the IDR, we replaced all the tryptophans in the IDR of zfGal with tyrosines, which predominate in hGal3 (Fig. 4A). Comparing the HSQC spectra of this zfGal$^{W/Y}$ mutant and of its CRD alone (Fig. 4B), the most pronounced chemical shift perturbations occur on the CRD's NTD-binding face (Fig. 4C). Furthermore, the peak intensities from residues on the NTD-binding face are less pronounced in the spectra of zfGal$^{W/Y}$ than they are in the spectrum of wild-type zfGal (Fig. 4D,E). These results indicate increased intramolecular interactions between the disordered and structured domains in zfGal$^{W/Y}$. Nevertheless, concentration-dependent relaxation rate profiles (Fig. 4F) suggest that zfGal$^{W/Y}$ has a similar propensity for intermolecular self-association to wild-type zfGal's (see Fig. 3G; Table 1). The higher protein concentration of zfGal$^{W/Y}$ in the supernatant after LPS assays (Fig. 4G) suggests that the tyrosine-dominant construct in zfGal still has reduced agglutination capacities. Overall, therefore, these results suggest that the intermolecular self-association and agglutination capacity of IDR-bearing galectins is weakly dependent on the nature of aromatic residues in the IDR.

Effect of the number of aromatic motifs on agglutination

Another difference between zfGal and hGal3 is the number of repeated aromatic-containing motifs in the IDR (and its overall length). To investigate the importance of this factor, we engineered an NTD-augmented construct of zebrafish galectin (zfGal^{aug}, Fig. 5A), with six extra tryptophan-containing tetrapeptides to match the length and number of aromatic residues in the IDR of hGal3 (Fig. 5B). Reversible agglutination in LPS micelles was still observed (Fig. 5C). The chemical shift differences between zfGal^{aug} and the CRD alone suggest that intramolecular interactions are similar to those observed in wild-type zfGal (Fig. 5D), but less pronounced than those in zfGal$^{W/Y}$ (Fig. 4C). However, zfGal^{aug} samples precipitated rapidly, and the low concentration (40 μM) NMR spectrum showed significant line broadening compared with that of wild-type zfGal (Appendix Fig. S4). Furthermore, while according to the length of their IDRs, the dynamic properties of zfGal3^{aug} should be similar to those of hGal3 (ignoring self-association), the R_2 values measured at a concentration of 40 μM are higher than those measured in hGal3 at the same concentration (Fig. 5E), indicating a greater tendency toward intermolecular self-association. Meanwhile, LPS micelle assays indicated that zfGal^{aug}'s agglutination capacity is much higher than wild-type zfGal's (Fig. 5F; nearly no protein detected in the supernatant). The increased agglutination ability of zfGal^{aug} relative to hGal3, despite their same IDR length and number of aromatic residues, is perhaps due to differences in the spacing of aromatic motifs in their IDRs that affect the strength of multivalent assembly (Martin et al, 2020; Holehouse et al, 2021) and solubility (Farag et al, 2022). These findings, therefore, indicate that the number of aromatic residues in the IDR is a more important determinant of galectin self-association and agglutination than the nature of these aromatic residues.

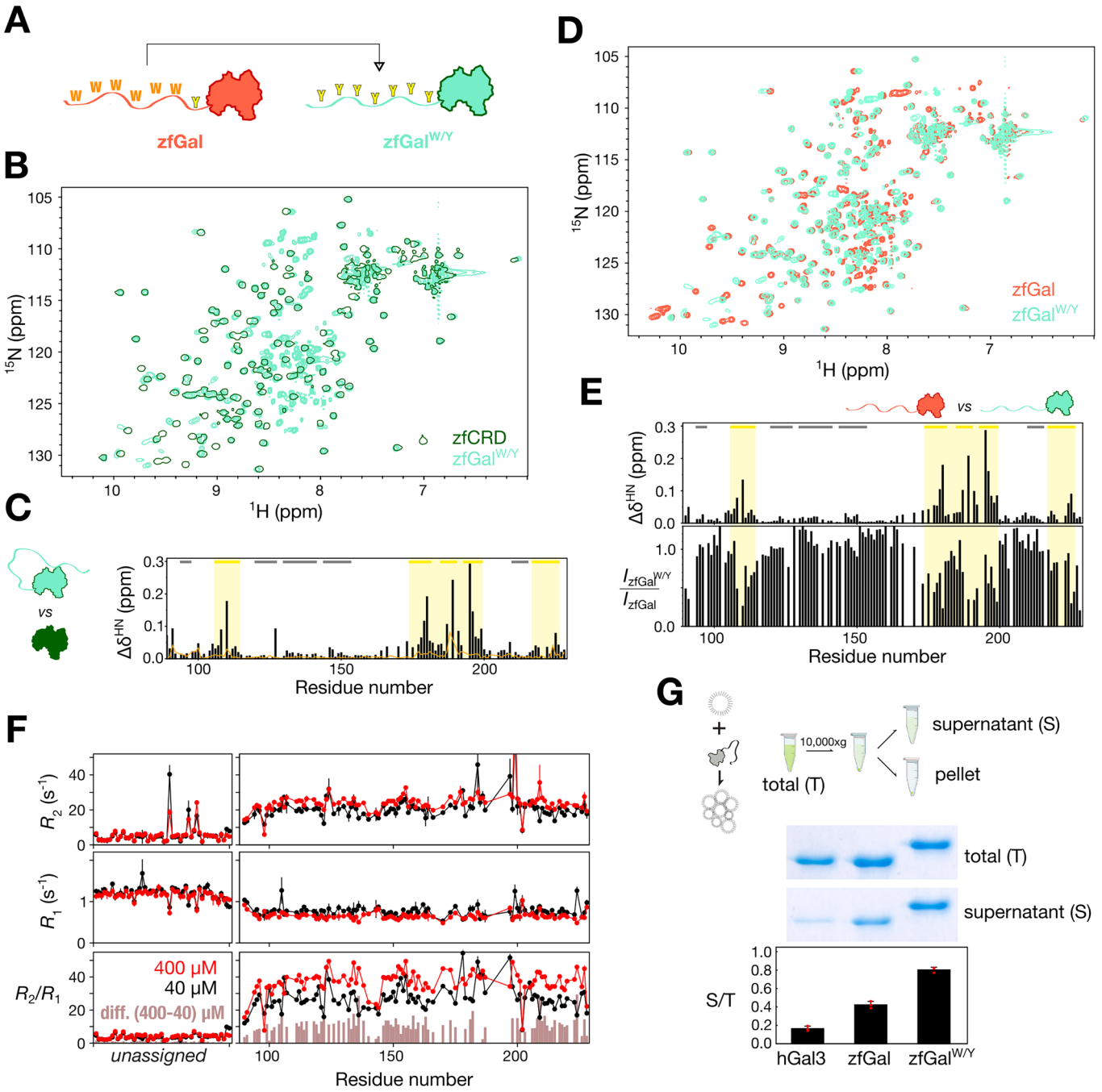

Figure 4. Effects on self-assembly of aromatic residue type in zebrafish galectin.

(**A**) Schematic illustration of the replacement of the tryptophans in zebrafish galectin's intrinsically disordered N-terminal domain (NTD) with tyrosines, yielding the zfGal$^{W/Y}$ construct. (**B**) Overlaid HSQC spectra of full-length (light green) zfGal$^{W/Y}$ and its carbohydrate-recognition domain (CRD) alone (dark green), and (**C**) the corresponding average chemical shift perturbations between the two (black bars). The orange line is the same comparison for wild-type zfGal (as shown in Fig. 3D). (**D**) Overlaid HSQC spectra of full-length zfGal$^{W/Y}$ (green) and wild-type zfGal (orange), and corresponding (**E**) average chemical shift differences and intensity ratios. Residues on the NTD interacting side of the CRD are highlighted in yellow. (**F**) Transverse (R_2) and longitudinal (R_1) relaxation rate constants and R_2/R_1 ratio as a function of residue number (the NTD is unassigned) measured in 400 μM (red) and 40 μM (black) samples of zfGal$^{W/Y}$. Error bars indicate ±1 standard deviation (1σ) of the fitted R_1 and R_2 values estimated by Monte Carlo analysis (see Methods). The brown bars are the difference in R_2/R_1 ratios between high and low concentrations. (**G**) Schematic illustration of lipopolysaccharide (LPS) agglutination assays. Representative SDS-PAGE analysis and protein amounts in the supernatant (S) of centrifuged LPS/protein mixtures determined by Bradford assays normalized to the total (T) amount of protein added for wild-type human galectin-3 (hGal3), zfGal$^{W/Y}$, and zfGal. Measurements were performed in triplicate, and results are reported as mean ± s.d. Source data are available online for this figure.

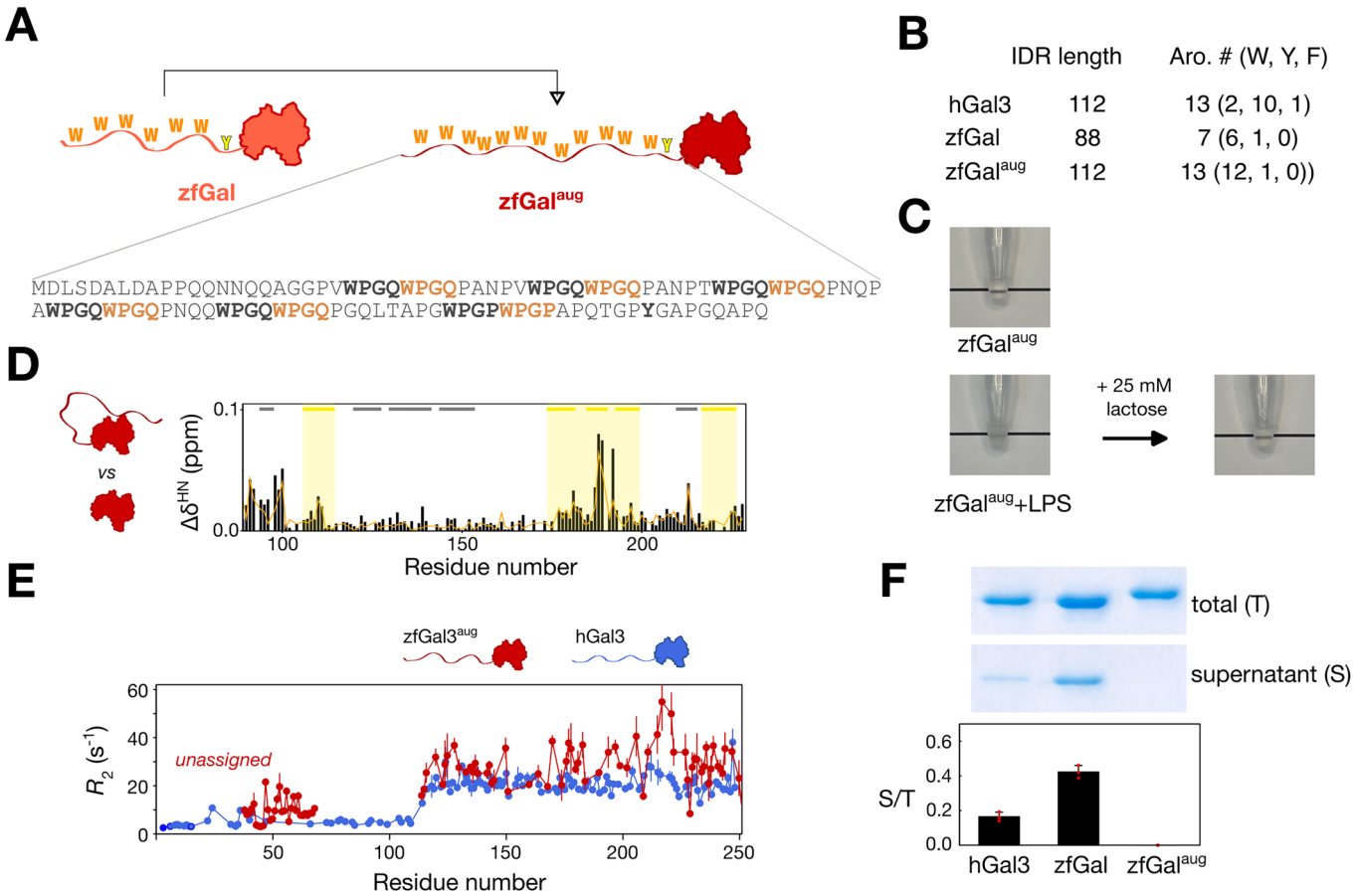

Figure 5. Effects on self-assembly of the number of aromatic-containing motifs in zebrafish galectin.

(**A**) Six tetrapeptides in the native sequence (bold font) of zebrafish galectin (zfGal) were duplicated to extend the intrinsically disordered region (IDR), yielding the zfGal^{aug} construct. (**B**) Comparison of the lengths and number of aromatic residues in the IDRs of human galectin-3 (hGal3), zfGal, and zfGal^{aug}. (**C**) Photographs of zfGal^{aug} samples becoming turbid after mixing with lipopolysaccharide (LPS) micelles (left) and becoming transparent once more after adding lactose (right). (**D**) Chemical shift differences between the presence and absence of the IDR of zfGal^{aug}. The orange line is the same comparison for wild-type zfGal (as shown in Fig. 3D). (**E**) Transverse relaxation rate constants (R_2) in 40 μM samples of zfGal^{aug} (red) and hGal3 (blue). (**F**) Representative SDS-PAGE analysis and protein amounts in the supernatant (S) of centrifuged LPS/protein mixtures determined by Bradford assays normalized to the total (T) amount of protein added for hGal3, zfGal (the same data as in Fig. 4G), and zfGal^{aug}. Measurements were performed at least in triplicate, and results are reported as mean ± s.d. Source data are available online for this figure.

Contribution to self-association of the conserved N-terminal fragment

Apart from the repeated motifs on the same species, the motif analysis also revealed that the N-terminal residues of the IDRs are conserved across vertebrates (Fig. 1G). To investigate the role of this conserved fragment, we constructed a human CRD tethered to the first 21 residues of the NTD (a truncated construct without IDR residues 22–113; hGal3$^{\Delta 22-113}$). Although the agglutination ability of hGal3$^{\Delta 22-113}$ was similar to the CRD-only construct (Appendix Fig. S5), the R_2s of hGal3$^{\Delta 22-113}$ still increased between protein concentrations of 40 and 400 μM (Fig. 6A). This increase was greater than observed for the CRD alone (compare the brown bars ΔR_2 in Fig. 6A,B). Per-residue difference-of-differences in transverse relaxation rate $[\Delta\Delta R_2 = \Delta R_2(\text{hGal3}^{\Delta 22-113}) - \Delta R_2(\text{hCRD})]$ are mostly positive and a one-sided sign test rejects the null hypothesis that the median $\Delta\Delta R_2$ is zero (Fig. 6D). These analyses indicate that the observed R_2 enhancement in hGal3$^{\Delta 22-113}$ construct is a true effect and not attributable to random noise or variability, suggesting that the conserved fragment promotes self-assembly. Similar increases in R_2s were also observed in a construct with IDR aromatic residues replaced by glycines (hGal3$^{WY/G}$; Fig. 6C), which has no agglutination capacity because the substituted aromatic residues provide the π-π and cation-π interactions required for PS (Chiu et al, 2020; Sun et al, 2024). The similar R_2 increments in these two constructs support the involvement of the conserved fragment in self-association. The HSQC spectra of hGal3$^{WY/G}$ and hGal3$^{\Delta 22-113}$ show similar chemical shift perturbations relative to the CRD-only construct (Fig. 6D,E; Appendix Fig. S6), which likewise suggests that the interactions involve the N-terminal residues. The perturbations in these constructs are most pronounced in β-strands 2 and 11 (Fig. 6F), rather than in β-strands 7–9 for wild-type hGal3 (Fig. 3E). Contacts between this short fragment and these two β-strands may contribute to the observed weak self-association.

Discussion

Sequence duplication is one of the most primordial modes of protein evolution (Lupas et al, 2001; Soding and Lupas, 2003; Kashi and King,

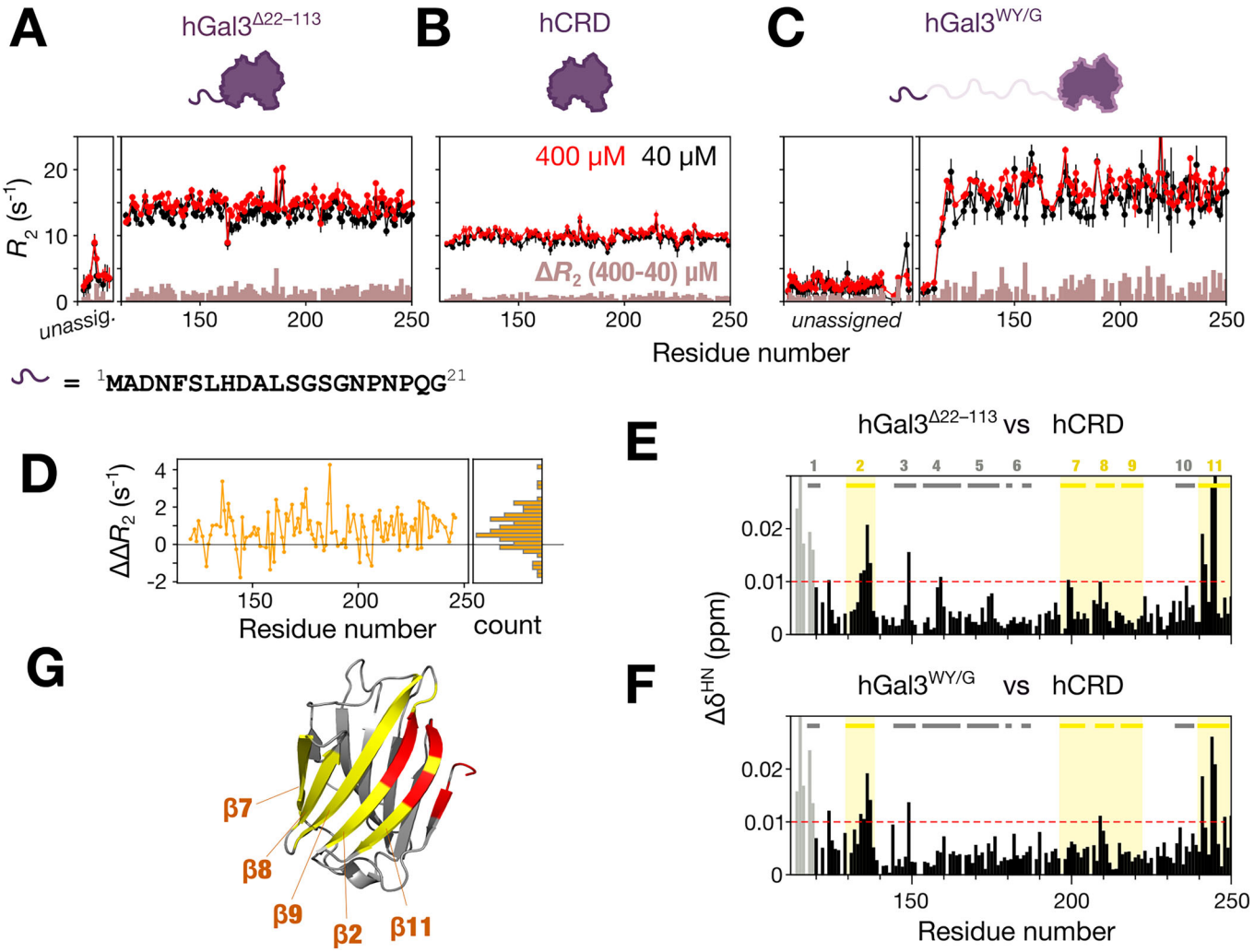

Figure 6. Contribution to self-association of the conserved N-terminal motif in IDR-tethered galectins.

(**A–C**) Transverse relaxation rate constants (R_2) of 400 μM (red) and 40 μM (black) samples of (**A**) human galectin-3 with only the first 21 residues of the IDR present (hGal3$^{\Delta 22-113}$), (**B**) a structured domain-only (CRD-only) construct, and (**C**) a construct with tryptophans and tyrosines in the intrinsically disordered region replaced by glycine (hGal3$^{WY/G}$). Error bars indicate ±1 standard deviation (1σ) of the fitted R_2 values estimated by Monte Carlo analysis (see Methods). The differences between the two concentrations are shown as brown bars. (**D**) Per-residue difference-of-differences in transverse relaxation rate [$\Delta\Delta R_2 = \Delta R_2$(hGal3$^{\Delta 22-113}$) − ΔR_2(hCRD)]. The histogram (right panel) shows the distribution of $\Delta\Delta R_2$ values. A one-sided sign test rejects the null hypothesis of no shift ($p = 7.1 \times 10^{-12}$). The chemical shift perturbation (**E**) between hGal3$^{\Delta 22-113}$ and the CRD-only construct and (**F**) between hGal3$^{WY/G}$ and the CRD-only construct. The perturbations in the N-terminus of the structured domain are due to sequence variations (gray bars). (**G**) Residues with chemical shift perturbations greater than 0.01 ppm (an arbitrary threshold for indicating the most pronounced perturbations) are highlighted in red on a structural model of the CRD. Source data are available online for this figure.

2006; Alva et al, 2015), as highlighted in the seminal work of Eck and Dayhoff (Eck and Dayhoff, 1966), which explains the emergence of a folded protein from repeated short motifs introduced via structure-promoting amino acids (e.g., cysteine or tryptophan). Large-scale gene duplications over many generations create paralogs in genomes, offering opportunities for new functions to evolve, leading over time to the development of highly specialized folded proteins (Ohno, 1970; Britten, 2006; Innan and Kondrashov, 2010). The evolution of protein does not stop at a structured form. As complicated cells, such as eukaryotic cells and multicellular organisms, have evolved, a protein could have "moonlight" (Jeffery, 1999) multiple functions, with the need for spatiotemporal controls for various functions. The emergence of IDRs with distinct physicochemical properties fulfills such requirements, notably through PS (Pritisanac et al, 2020; Holehouse and Kragelund, 2024). While there may be many pathways for IDRs to evolve, motif duplication would represent a relatively straightforward route (Lupas et al, 2001; Soding and Lupas, 2003; Kashi and King, 2006; Alva et al, 2015), consistent with our observation for galectins.

Galectin-3's CRD is widely distributed in diverse organisms, as evidenced by the ~17,000 sequences in Fig. 1A and reference (Cooper and Barondes, 1999). Our analysis further reveals that these homologs can also evolve with IDRs (Fig. 1; Dataset EV2). Notably, these IDRs are not always tethered to the N-terminal region of a CRD. For instance, in one plant example, the IDR is tethered to the C-terminal region, whereas in nematode examples, IDRs are attached to tandem-repeated CRDs (Appendix Fig. S7;

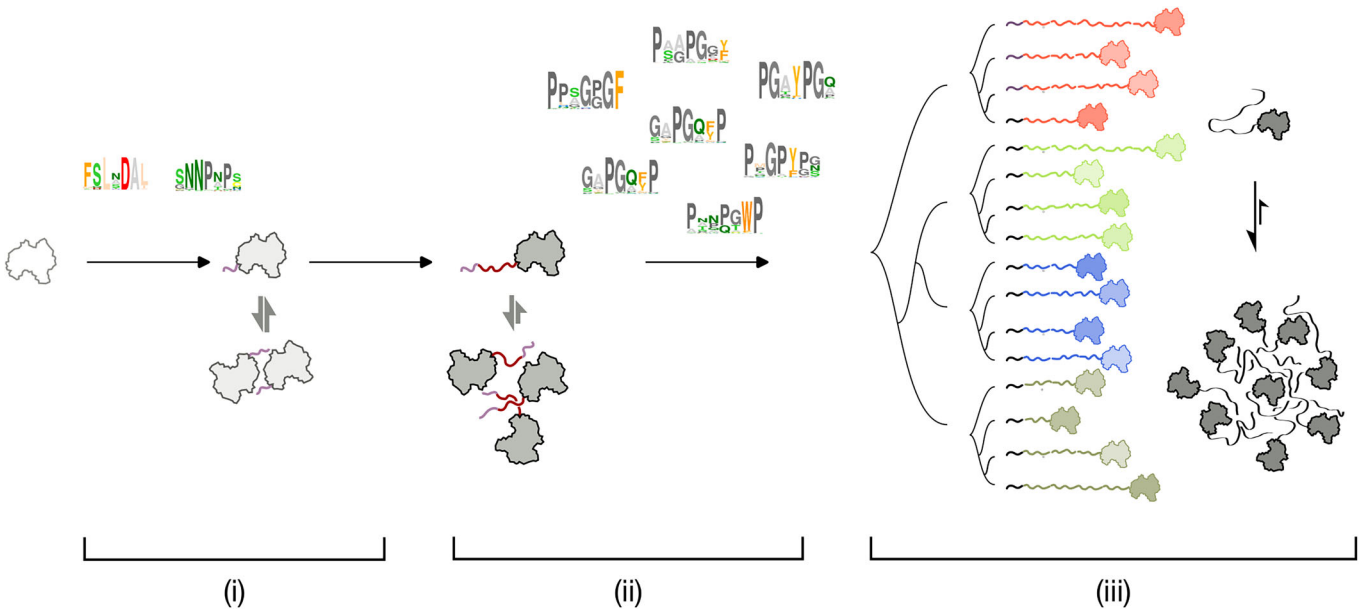

Figure 7. Proposed evolutionary route for IDR-tethered galectin.

(i) An ancestral galectin, harboring a single carbohydrate-recognition domain (CRD), acquires an incipient fragment (light purple) that facilitates self-association. (ii) An aromatic residue-containing motif (dark purple) inserted into this fragment, diversifying over time in both the aromatic residue types and the motif context. (iii) Different lineages fix the type(s) of aromatic residues in these motifs and then independently duplicate them, producing varying numbers of repeats. Natural selection fine-tunes the number of repeats for the fitness of assembly strength.

Dataset EV2). Their diverse amino acid compositions, variable lengths, and differing N-/C-terminal positions indicate that these IDRs have likely evolved independently across distinct lineages (Fig. 1B; Appendix Fig. S7).

Interestingly, while vertebrate's galectin IDRs share similar overall amino acid compositions, the specific types of aromatic residues differ (Fig. 1C). For example, the IDR-tethered galectin of zebrafish is rich in tryptophans rather than tyrosines in human's galectin-3 (Fig. 2). Our results indicate that the reduced self-assembly and agglutination ability of this zebrafish galectin (Fig. 3) is not due to this difference in amino acid type (Fig. 4), but rather to the number of repeated aromatic motifs in the amino acid sequence (Fig. 5). While recent studies have highlighted the role of aromatic residues in driving PS by acting as "stickers" (Wang et al, 2018; Bremer et al, 2022), our findings suggest that natural selection does not always favor a specific type of aromatic residue. One of the possible reasons may stem from the interactions between NTD and CRD. As demonstrated in our previous NMR analyses, positively charged residues on the CRD's non-ligand-binding surface (the NTD-binding face) contribute to overall assembly via cation-π interactions (Sun et al, 2024). Although the zebrafish CRD is conserved relative to the human ortholog, the number and spatial arrangement of these basic residues differ. Consequently, replacing tryptophans with tyrosines does not necessarily enhance assembly strength, as might be expected from model peptide studies. Instead, our data suggest that the evolutionary optimization of galectin assembly is achieved not by selecting the strongest individual "sticker" residue, but by duplicating the aromatic residue-containing motif multiple times, which seems to be the more efficient evolutionary strategy.

Different repeated motifs in IDRs may provide adaptive advantages. Fish, inhabiting environments spanning from cold to warm and from fresh to more or less salty, represent the most diverse class of vertebrates. Although fish have undergone multiple gene duplication events during their evolution history (Meyer and Schartl, 1999), our analysis reveals that they also exhibit the greatest variation in galectin IDR lengths among vertebrates (Appendix Fig. S8). Furthermore, while the correlation between the number of aromatic residues in fish galectin IDRs and living environments is not clear, fish generally have more IDR-tethered galectins than other vertebrates (Appendix Fig. S8). It is plausible that galectins with various IDR lengths may have evolved in fish as an adaptation to environmental changes. For example, multiple copies of IDR-tethered galectins in trout and salmon with different numbers of aromatic motif repeats (Appendix Fig. S8) may have evolved as adaptations to their life cycle during which they transit between fresh, brackish, and salt water.

Human galectin-3, a β-galactoside-binding lectin, is unique among the galectin family for not being in dimer or tandem-repeat form (Yang et al, 2008). Phylogenetic analysis showed that a CRD-only structure as a common ancestor (Houzelstein et al, 2004) may have been duplicated in tandem-repeat form (e.g., human galectin-4 and -8) or have been selected through mutations that promote dimerization (e.g., human galectin-1 and -2). How, then, did galectin-3's unique chimeric form with a long-disordered region emerge? It is unlikely that the IDR originated through "destructuring" of a CRD because the IDR sequence differs substantially from other tandem-repeat galectins. Instead, the conserved N-terminal sequence found in vertebrate galectins, which promotes self-association (Fig. 6), may have seeded the eventual emergence of extended IDRs. This early conserved fragment might have played an evolutionary role analogous to that of the functional shift of a "2% wing" in the emergence of avian flight (Gould, 1985) or to the incidental assembly of an enzyme or chaperon in the developing lens of animal eyes (Shimeld et al, 2005; Piatigorsky, 2006). Over time, short aromatic-containing motifs were appended to

this incipient fragment to facilitate assembly. These motifs likely diversified and were independently duplicated in different species, ultimately creating varying numbers of repeats. Environmental pressures would then have fine-tuned these repeats to optimize agglutination strength in each species, thereby shaping the evolution of galectin IDRs in vertebrates (Fig. 7).

In this proteome-wide investigation focused on human galectin-3, instead of using homolog databases based on sequence or functional similarity, we specifically identified galectins with long IDRs and explored their evolutionary paths from fish to humans. Our findings suggest that the inherent sequence diversity of IDRs is crucial to their evolutionary adaptability, and this insight advances our understanding of the molecular basis of evolutionary biology, bringing our another "inner fish" (Shubin, 2008) to the fore.

Methods

Reagents and tools table

Reagent/resource	Reference or source	Identifier or catalog number
Chemicals, enzymes and other reagents		
Acetic acid	J.T.Baker	9508 03
Acetone	Honeywell	32201
Agar	BioShop Canada, Inc.	AGR001.1
Agarose	UniRegion	UR-AGA001
Ammonium chloride (NH_4Cl)	Sigma-Aldrich	213330 500 G
Ammonium chloride (^{15}N, 99%)	Cambridge Isotope Laboratories, Inc.	NLM-467-1
Ammonium persulfate (APS)	Sigma-Aldrich	A3678-25G
Ampicillin sodium salt	Gold Biotechnology, Inc.	A-301-100
Bromophenol blue	BioShop Canada, Inc.	BRO777
Basal Medium Eagle (BME) Vitamin Concentrate 100x Powder	United States Biological, Inc.	B0110
Calcium chloride anhydrous	Sigma-Aldrich	C4901-100G
Coomassie Brilliant Blue G	Sigma-Aldrich	B-0770
Coomassie brilliant blue G250	Merck	1.15444.0025
cOmplete Protease Inhibitor Cocktail	Roche	000000005892791001
Deoxyribonuclease I (DNase I)	Bionovas	DRB001.100
Deuterium oxide, 99.9 atom % D, contains 0.75 wt. % 3-(trimethylsilyl) propionic-*2,2,3,3-d*$_4$acid, sodium salt	Sigma-Aldrich	293040-25 G
D-(+)-Glucose	Sigma-Aldrich	G5767-500G
D-Glucose (U-^{13}C6, 99%)	Cambridge Isotope Laboratories, Inc.	CLM-1396-1
Ethanol	J.T.Baker	8006-05
Ethylenediaminetetraacetic acid (EDTA)	Sigma-Aldrich	E4884-100G
Glycerol	BioShopCanada, Inc.	GLY001.1
Glycine	J.T.Baker	4059-06
Imidazole	Alfa Aesar	A10221
Isopropanol	J.T.Baker	9084-03
Isopropyl β-D-1-thiogalactopyranoside (IPTG)	Gold Biotechnology, Inc.	I2481C100
Lactose	Sigma-Aldrich	5989-81-1
Lipopolysaccharide from *E. coli* serotype 055:B5 (LPS)	Sigma-Aldrich	SI-L2880-10MG
Lysozyme	BIONOVAS	AL0680-0010
Magnesium chloride anhydrous	Sigma-Aldrich	M-8266-100G
Magnesium sulfate heptahydrate	Sigma-Aldrich	230391-500 G
Methanol	Macron Fine Chemicals	3016.68
Phenylmethylsulfonyl fluoride (PMSF)	Sigma-Aldrich	P7626-5G
Potassium chloride	Sigma-Aldrich	P3911-500G
Potassium phosphate monobasic	Sigma-Aldrich	P5379-500G
RNase A	Sigma-Aldrich	R5503-100MG
Sodium chloride	Sigma-Aldrich	31434-5KG-R
Sodium chloride	VWR Life Science	0241-1KG
Sodium hydroxide	Sigma-Aldrich	30620
Sodium phosphate dibasic dihydrate	Sigma-Aldrich	04272-1KG
Sodium phosphate monobasic	Sigma-Aldrich	S0751-500G
Sodium dodecyl sulfate (SDS)	Sigma-Aldrich	75746-1KG
Tris hydroxymethyl aminomethane (Tris-base)	Bioman	TRS011
Tryptone	Bioshop Canada, Inc.	TRP402.1
Yeast extract	Bioshop Canada, Inc	YEX401.500
Mini Plus Plasmid DNA Extraction System	Viogene	GF2001
Gel/PCR DNA Isolation System	Viogene	GP1001
100 bp DNA Ladder	Bioman	DL100
1 kb DNA Ladder	Bioman	DL1000
Gel Loading Dye (6X)	New England Biolabs, Inc.	B7024S
Acrylamide/Bis Acrylamide (29:1) 30% Solution	BioShopCanada, Inc.	ACR009.500
DNA View	BioTools	TT-DNA01
Prestained Protein Molecular Weight Marker	Bioman	Prep1025
DpnI	New England Biolabs, Inc.	R0176S

Reagent/resource	Reference or source	Identifier or catalog number
Q5 High-Fidelity 2X Master Mix	New England Biolabs, Inc.	M0492S
T4 DNA Ligase	New England Biolabs, Inc.	M0202S
Bacterial Strains		
ECOSTM 101 *E. coli* Competent Cells [DH5α]	Yeastern Biotech Co.,Ltd.	LYE678-80VL
ECOSTM 21 *E. coli* Competent Cells [BL21 (DE3)]	Yeastern Biotech Co.,Ltd.	FYE207-40VL
Rosetta™ (DE3) Competent Cells-Novagen	Sigma-Aldrich	70954
Recombinant DNA		
His_6-SUMO-hGal3	Lin et al, 2017	N/A
His_6-SUMO-hGal3$^{WY/G}$	Chiu et al, 2020	N/A
His_6-SUMO-hGal3$^{Y/W}$	Gene synthesis (Synbio)	N/A
His_6-SUMO-hGal3$^{\Delta 22\text{-}113}$	This work	N/A
His_6-SUMO-hGal3$^{\Delta 20}$	Lin et al, 2017	N/A
His_6-SUMO-zfGal3	Gene synthesis (Gene Script Inc.)	N/A
His_6-SUMO-zfCRD	This work	N/A
His_6-SUMO-zfGal3$^{W/Y}$	Gene synthesis (Gene Script Inc.)	N/A
His_6-SUMO-zfGal3^{aug}	Gene synthesis (Gene Script Inc.)	N/A
Software and algorithms		
BeStSel	https://bestsel.elte.hu/information.php	
AlphaFold	https://alphafoldserver.com/	
PLAAC	http://plaac.wi.mit.edu/	
PONDR	http://www.pondr.com/	
PScore	http://abragam.med.utoronto.ca/~JFKlab/Software/psp.htm	
FuzDrop	https://fuzdrop.bio.unipd.it/predictor	
ProtParam	https://web.expasy.org/protparam/	
NMRPipe	https://www.ibbr.umd.edu/nmrpipe/	
Sparky	https://nmrfam.wisc.edu/nmrfam-sparky-distribution/	
I-PINE	http://i-pine.nmrfam.wisc.edu/	
NMRtist	https://nmrtist.org/	
PyMOL	https://pymol.org/	
Table of primer		
Construct name	**Template**	**primer**
His-SUMO-zfCRD	His-SUMO -zfGal3	F: 5′ attggcggcggacaagctccacaagtg 3′ R: 5′ agcttgtccgccgccaatctgttctct 3′
His-SUMO-hGal3$^{\Delta 22\text{-}113}$	His-SUMO-hGal3	F: 5′ caggaccactgattgtgccttataacctg 3′ R: 5′ cagtggtccttgagggtttgggtttccaga 3′

Bioinformatics and sequence analysis

Protein sequence databases were obtained from the trEMBL database (accessed February 2023) (UniProt 2023). The BLAST (Basic Local Alignment Search Tool) (Zaru et al, 2023) algorithm was run locally to identify similar sequences. IUPRED3 (Erdos et al, 2021) was integrated with in-house written Python scripts designed to select proteins based on the length of their disordered regions. The species of the selected protein was retrieved from the corresponding FASTA file, and the phylogenetic relations were generated using the ete3 toolkit (Huerta-Cepas et al, 2016). MEME suite (motif-based sequence analysis tools) (Bailey et al, 2015) was applied to search sequence motifs.

Levels of structural disorder and prion-likeness were respectively estimated with the PONDR (Obradovic et al, 2005) and PLAAC (Lancaster et al, 2014) webservers. π-π interactions and PS were predicted using the PScore predictor (Vernon et al, 2018) and the FuzDrop server (Hardenberg et al, 2020). The structure of the CRD of IDR-tethered zebrafish galectin was predicted using AlphaFold (Jumper et al, 2021), accessed through the ColabFold interface (Mirdita et al, 2022).

DNA constructs

The construction of plasmids for full-length, CRD-only, and aromatic residues-removed (WY/G) human galectin-3 has been described previously (Lin et al, 2017; Chiu et al, 2020). The construct with only the 21 N-terminal residues of the IDR present (hGal3$^{\Delta 22-113}$) was designed using the FastCloning (Li et al, 2011) method. The cDNA sequences of IDR-tethered zebrafish galectin (zfGal, zfGal$^{W/Y}$, and zfGal^{aug}) were created by whole gene synthesis (Gene Script Inc. and Synbio). A hexahistidine-tagged small ubiquitin-like modifier protein (His_6-SUMO) was used in each case to assist purification. All constructs were confirmed by sequencing.

Protein purification and NMR data collection

All variants used in this study were purified as previously described (Lin et al, 2017; Chiu et al, 2020; Sun et al, 2024). NMR data, including HSQC spectral intensity, chemical shift analysis, chemical shift assignment, and transverse (R_2) and longitudinal (R_1) relaxation rate constants, were collected and analyzed following established protocols (Lin et al, 2017; Chiu et al, 2020; Sun et al, 2024). Detailed procedures are provided in the Appendix Methods.

Circular dichroism analysis

Circular dichroism (CD) spectra were recorded on an AVIV model 410 spectropolarimeter at 303 K. Samples were loaded into a 0.1 mm cuvette. Ten measurements were co-added for each data point, between 190 and 260 nm, with an interval of 1 nm. The CD signal was normalized to the sample concentration and the number of residues. The measured theta machine units (θ) were converted to Δε using the following equation:(Greenfield, 2006)

$$\triangle\varepsilon = \theta \cdot \frac{0.1 \cdot MRW}{l \cdot C \cdot 3298}$$

where l is the path length (in cm), C is the protein concentration (in mg/ml), and MRW is the mean residue weight (molecular weight/residue number, in Dalton). Secondary structure populations were estimated using the BeStSel program (Micsonai et al, 2015; Micsonai et al, 2018). All measurements were conducted in three independent replicates.

Lipopolysaccharide (LPS) agglutination assays

Lipopolysaccharide micelles from *E. coli* strain O55:B5 were obtained from Merck (Catalog No. L2880). A total amount of 20 µM protein (T) was mixed with a final concentration of 0.2 mg/ml LPS, which was then centrifuged at 10,000×*g* for 5 min to obtain the supernatant (S) and pellet. Protein concentrations (S, T) were determined using Bradford assays. Bovine serum albumin (BSA) standards and the assay samples were mixed with 170 µl of Bradford reagent, and the absorbance at 594 and 466 nm (A594 and A466) was measured using a TECAN Spark microplate reader. Sample concentrations were obtained from a linear regression of BSA concentrations as a function of A594/A466 ratios (Zor and Selinger, 1996). SDS-PAGE analyses were also performed to confirm the amount and integrity of the samples. All measurements were performed at least in triplicate.

Data availability

All data and codes/scripts for analysis were deposited as the Source Data with this article online. The chemical shifts reported in this article are deposited in the Biological Magnetic Resonance Bank (BMRB) with the access number 52443. (https://bmrb.io/data_library/summary/index.php?bmrbId=52443).

The source data of this paper are collected in the following database record: biostudies:S-SCDT-10_1038-S44319-026-00692-w.

Expanded view data, supplementary information, appendices are available for this paper at https://doi.org/10.1038/s44319-026-00692-w.

Peer review information

A peer review file is available at https://doi.org/10.1038/s44319-026-00692-w

References

Akdel M, Pires DEV, Pardo EP, Janes J, Zalevsky AO, Meszaros B, Bryant P, Good LL, Laskowski RA, Pozzati G et al (2022) A structural biology community assessment of AlphaFold2 applications. Nat Struct Mol Biol 29:1056–1067

Akerud T, Thulin E, Van Etten RL, Akke M (2002) Intramolecular dynamics of low molecular weight protein tyrosine phosphatase in monomer-dimer equilibrium studied by NMR: a model for changes in dynamics upon target binding. J Mol Biol 322:137–152

Altenhoff AM, Train CM, Gilbert KJ, Mediratta I, Mendes de Farias T, Moi D, Nevers Y, Radoykova HS, Rossier V, Warwick Vesztrocy A et al (2021) OMA orthology in 2021: website overhaul, conserved isoforms, ancestral gene order and more. Nucleic Acids Res 49:D373–D379

Alva V, Soding J, Lupas AN (2015) A vocabulary of ancient peptides at the origin of folded proteins. Elife 4:e09410

Bailey TL, Johnson J, Grant CE, Noble WS (2015) The MEME suite. Nucleic Acids Res 43:W39–W49

Banani SF, Lee HO, Hyman AA, Rosen MK (2017) Biomolecular condensates: organizers of cellular biochemistry. Nat Rev Mol Cell Biol 18:285–298

Baryshnikova OK, Sykes BD (2006) Backbone dynamics of SDF-1alpha determined by NMR: interpretation in the presence of monomer-dimer equilibrium. Protein Sci 15:2568–2578

Bremer A, Farag M, Borcherds WM, Peran I, Martin EW, Pappu RV, Mittag T (2022) Deciphering how naturally occurring sequence features impact the phase behaviours of disordered prion-like domains. Nat Chem 14:196–207

Britten RJ (2006) Almost all human genes resulted from ancient duplication. Proc Natl Acad Sci USA 103:19027–19032

Capra JA, Singh M (2007) Predicting functionally important residues from sequence conservation. Bioinformatics 23:1875–1882

Chiu SH, Ho WL, Sun YC, Kuo JC, Huang JR (2022) Phase separation driven by interchangeable properties in the intrinsically disordered regions of protein paralogs. Commun Biol 5:400

Chiu YP, Sun YC, Qiu DC, Lin YH, Chen YQ, Kuo JC, Huang JR (2020) Liquid-liquid phase separation and extracellular multivalent interactions in the tale of galectin-3. Nat Commun 11:1229

Cooper DN, Barondes SH (1999) God must love galectins; he made so many of them. Glycobiology 9:979–984

Dasmeh P, Doronin R, Wagner A (2021) The length scale of multivalent interactions is evolutionarily conserved in fungal and vertebrate phase-separating proteins. Genetics 220:iyab184

Dasmeh P, Wagner A (2021) Natural selection on the phase-separation properties of FUS during 160 My of mammalian evolution. Mol Biol Evol 38:940–951

Dunker AK, Obradovic Z, Romero P, Garner EC, Brown CJ (2000) Intrinsic protein disorder in complete genomes. Genome Inform Ser Workshop Genome Inform 11:161–171

Eck RV, Dayhoff MO (1966) Evolution of the structure of ferredoxin based on living relics of primitive amino acid sequences. Science 152:363–366

Erdos G, Pajkos M, Dosztanyi Z (2021) IUPred3: prediction of protein disorder enhanced with unambiguous experimental annotation and visualization of evolutionary conservation. Nucleic Acids Res 49:W297–W303

Farag M, Cohen SR, Borcherds WM, Bremer A, Mittag T, Pappu RV (2022) Condensates formed by prion-like low-complexity domains have small-world network structures and interfaces defined by expanded conformations. Nat Commun 13:7722

Fushman D, Cahill S, Cowburn D (1997) The main-chain dynamics of the dynamin pleckstrin homology (PH) domain in solution: analysis of 15N relaxation with monomer/dimer equilibration. J Mol Biol 266:173–194

Gonzalez-Foutel NS, Glavina J, Borcherds WM, Safranchik M, Barrera-Vilarmau S, Sagar A, Estana A, Barozet A, Garrone NA, Fernandez-Ballester G et al (2022) Conformational buffering underlies functional selection in intrinsically disordered protein regions. Nat Struct Mol Biol 29:781–790

Gould SJ (1985) Not necessarily a wing. Nat Hist 94:12–25

Greenfield NJ (2006) Using circular dichroism spectra to estimate protein secondary structure. Nat Protoc 1:2876–2890

Hardenberg M, Horvath A, Ambrus V, Fuxreiter M, Vendruscolo M (2020) Widespread occurrence of the droplet state of proteins in the human proteome. Proc Natl Acad Sci USA 117:33254–33262

Harmon TS, Holehouse AS, Rosen MK, Pappu RV (2017) Intrinsically disordered linkers determine the interplay between phase separation and gelation in multivalent proteins. Elife 6:e30294

Ho WL, Huang HC, Huang JR (2023) IFF: Identifying key residues in intrinsically disordered regions of proteins using machine learning. Protein Sci 32:e4739

Ho WL, Huang JR (2022) The return of the rings: Evolutionary convergence of aromatic residues in the intrinsically disordered regions of RNA-binding proteins for liquid-liquid phase separation. Protein Sci 31:e4317

Holehouse AS, Ginell GM, Griffith D, Boke E (2021) Clustering of aromatic residues in prion-like domains can tune the formation, state, and organization of biomolecular condensates. Biochemistry 60:3566–3581

Holehouse AS, Kragelund BB (2024) The molecular basis for cellular function of intrinsically disordered protein regions. Nat Rev Mol Cell Biol 25:187–211

Holehouse AS, Pappu RV (2018) Functional implications of intracellular phase transitions. Biochemistry 57:2415–2423

Hondele M, Sachdev R, Heinrich S, Wang J, Vallotton P, Fontoura BMA, Weis K (2019) DEAD-box ATPases are global regulators of phase-separated organelles. Nature 573:144–148

Houzelstein D, Goncalves IR, Fadden AJ, Sidhu SS, Cooper DN, Drickamer K, Leffler H, Poirier F (2004) Phylogenetic analysis of the vertebrate galectin family. Mol Biol Evol 21:1177–1187

Huerta-Cepas J, Serra F, Bork P (2016) ETE 3: reconstruction, analysis, and visualization of phylogenomic data. Mol Biol Evol 33:1635–1638

Innan H, Kondrashov F (2010) The evolution of gene duplications: classifying and distinguishing between models. Nat Rev Genet 11:97–108

Jayaraman V, Toledo-Patino S, Noda-Garcia L, Laurino P (2022) Mechanisms of protein evolution. Protein Sci 31:e4362

Jeffery CJ (1999) Moonlighting proteins. Trends Biochem Sci 24:8–11

Jemth P, Karlsson E, Vogeli B, Guzovsky B, Andersson E, Hultqvist G, Dogan J, Guntert P, Riek R, Chi CN (2018) Structure and dynamics conspire in the evolution of affinity between intrinsically disordered proteins. Sci Adv 4:eaau4130

Jensen MR, Kristensen SM, Keeler C, Christensen HE, Hodsdon ME, Led JJ (2008) Weak self-association of human growth hormone investigated by nitrogen-15 NMR relaxation. Proteins 73:161–172

Jumper J, Evans R, Pritzel A, Green T, Figurnov M, Ronneberger O, Tunyasuvunakool K, Bates R, Zidek A, Potapenko A et al (2021) Highly accurate protein structure prediction with AlphaFold. Nature 596:583–589

Karlsson E, Sorgenfrei FA, Andersson E, Dogan J, Jemth P, Chi CN (2022) The dynamic properties of a nuclear coactivator binding domain are evolutionarily conserved. Commun Biol 5:286

Kashi Y, King DG (2006) Simple sequence repeats as advantageous mutators in evolution. Trends Genet 22:253–259

Korchuganov DS, Nolde SB, Reibarkh MY, Orekhov VY, Schulga AA, Ermolyuk YS, Kirpichnikov MP, Arseniev AS (2001) NMR study of monomer-dimer equilibrium of barstar in solution. J Am Chem Soc 123:2068–2069

Lancaster AK, Nutter-Upham A, Lindquist S, King OD (2014) PLAAC: a web and command-line application to identify proteins with prion-like amino acid composition. Bioinformatics 30:2501–2502

Li C, Wen A, Shen B, Lu J, Huang Y, Chang Y (2011) FastCloning: a highly simplified, purification-free, sequence- and ligation-independent PCR cloning method. BMC Biotechnol 11:92

Lin YH, Qiu DC, Chang WH, Yeh YQ, Jeng US, Liu FT, Huang JR (2017) The intrinsically disordered N-terminal domain of galectin-3 dynamically mediates multisite self-association of the protein through fuzzy interactions. J Biol Chem 292:17845–17856

Lu AX, Lu AX, Pritisanac I, Zarin T, Forman-Kay JD, Moses AM (2022) Discovering molecular features of intrinsically disordered regions by using evolution for contrastive learning. PLoS Comput Biol 18:e1010238

Lupas AN, Ponting CP, Russell RB (2001) On the evolution of protein folds: are similar motifs in different protein folds the result of convergence, insertion, or relics of an ancient peptide world?. J Struct Biol 134:191–203

Martin EW, Holehouse AS, Peran I, Farag M, Incicco JJ, Bremer A, Grace CR, Soranno A, Pappu RV, Mittag T (2020) Valence and patterning of aromatic residues determine the phase behavior of prion-like domains. Science 367:694–699

Meyer A, Schartl M (1999) Gene and genome duplications in vertebrates: the one-to-four (-to-eight in fish) rule and the evolution of novel gene functions. Curr Opin Cell Biol 11:699–704

Micsonai A, Wien F, Bulyaki E, Kun J, Moussong E, Lee YH, Goto Y, Refregiers M, Kardos J (2018) BeStSel: a web server for accurate protein secondary structure prediction and fold recognition from the circular dichroism spectra. Nucleic Acids Res 46:W315–W322

Micsonai A, Wien F, Kernya L, Lee YH, Goto Y, Refregiers M, Kardos J (2015) Accurate secondary structure prediction and fold recognition for circular dichroism spectroscopy. Proc Natl Acad Sci USA 112:E3095–E3103

Mihalic F, Arcila D, Pettersson ME, Farkhondehkish P, Andersson E, Andersson L, Betancur RR, Jemth P (2024) Conservation of affinity rather than sequence underlies a dynamic evolution of the motif-mediated p53/MDM2 interaction in ray-finned fishes. Mol Biol Evol 41:msae018

Mirdita M, Schutze K, Moriwaki Y, Heo L, Ovchinnikov S, Steinegger M (2022) ColabFold: making protein folding accessible to all. Nat Methods 19:679–682

Obradovic Z, Peng K, Vucetic S, Radivojac P, Dunker AK (2005) Exploiting heterogeneous sequence properties improves prediction of protein disorder. Proteins 61:176–182

Ohno S (1970) Evolution by gene duplication. Springer

Pfuhl M, Chen HA, Kristensen SM, Driscoll PC (1999) NMR exchange broadening arising from specific low affinity protein self-association: analysis of nitrogen-15 nuclear relaxation for rat CD2 domain 1. J Biomol NMR 14:307–320

Piatigorsky J (2006) Evolutionary genetics: seeing the light: the role of inherited developmental cascades in the origins of vertebrate lenses and their crystallins. Heredity 96:275–277

Pritisanac I, Zarin T, Forman-Kay JD, Moses AM (2020) Whence blobs? Phylogenetics of functional protein condensates. Biochem Soc Trans 48:2151–2158

Shimeld SM, Purkiss AG, Dirks RP, Bateman OA, Slingsby C, Lubsen NH (2005) Urochordate betagamma-crystallin and the evolutionary origin of the vertebrate eye lens. Curr Biol 15:1684–1689

Shin Y, Brangwynne CP (2017) Liquid phase condensation in cell physiology and disease. Science 357:eaaf4382

Shubin N (2008) Your inner fish: a journey into the 3.5-billion-year history of the human body. Pantheon

Soding J, Lupas AN (2003) More than the sum of their parts: on the evolution of proteins from peptides. Bioessays 25:837–846

Sun YC, Hsieh TL, Lin CI, Shao WY, Lin YH, Huang JR (2024) A few charged residues in galectin-3's folded and disordered regions regulate phase separation. Adv Sci 11:e2402570

UniProt C (2023) UniProt: the Universal Protein Knowledgebase in 2023. Nucleic Acids Res 51:D523–D531

Vernon RM, Chong PA, Tsang B, Kim TH, Bah A, Farber P, Lin H, Forman-Kay JD (2018) Pi-Pi contacts are an overlooked protein feature relevant to phase separation. Elife 7:e31486

Wang J, Choi JM, Holehouse AS, Lee HO, Zhang X, Jahnel M, Maharana S, Lemaitre R, Pozniakovsky A, Drechsel D et al (2018) A molecular grammar governing the driving forces for phase separation of prion-like RNA binding proteins. Cell 174:688–699.e616

Waterhouse A, Bertoni M, Bienert S, Studer G, Tauriello G, Gumienny R, Heer FT, de Beer TAP, Rempfer C, Bordoli L et al (2018) SWISS-MODEL: homology modelling of protein structures and complexes. Nucleic Acids Res 46:W296–W303

Yang RY, Rabinovich GA, Liu FT (2008) Galectins: structure, function and therapeutic potential. Expert Rev Mol Med 10:e17

Zaru R, Orchard S, UniProt C (2023) UniProt tools: BLAST, align, peptide search, and ID mapping. Curr Protoc 3:e697

Zor T, Selinger Z (1996) Linearization of the Bradford protein assay increases its sensitivity: theoretical and experimental studies. Anal Biochem 236:302–308

Zuckerkandl E, Pauling L (1965) Evolutionary divergence and convergence in proteins. In: Bryson V, Vogel HJ (eds). Evolving genes and proteins. Academic Press, pp 97–166

Acknowledgements

This work was supported by the National Science and Technology Council of Taiwan (110-2113-M-A49A-504-MY3 and 113-2113-M-A49-031-MY3), Yen Tjing Ling Medical Foundation (CI-110-16 and CI-111-19), the Higher Education Sprout Project by the Ministry of Education (MOE) in Taiwan. Y-HL and Y-CS are the recipients of the Taiwan International Graduate Program (TIGP) Rising Star Fellowship. We thank Profs. Jun-Yi Leu and Yung-Che Tseng (Academia Sinica) for their insightful discussion. The authors also thank the Academia Sinica High-Field NMR Center (HFNMRC) for technical support. (HFNMRC is funded by Academia Sinica Core Facility and Innovative Instrument Project (AS-CFII-111-214).

Author contributions

Yu-Hao Lin: Conceptualization; Data curation; Formal analysis; Supervision; Investigation; Visualization; Writing—original draft. **Yu-Chen Chen**: Data curation; Formal analysis; Investigation; Visualization; Methodology; Writing—original draft. **Yung-Chen Sun**: Investigation. **Jie-rong Huang**: Conceptualization; Resources; Data curation; Software; Formal analysis; Supervision; Funding acquisition; Validation; Investigation; Visualization; Methodology; Writing—review and editing.

Source data underlying figure panels in this paper may have individual authorship assigned. Where available, figure panel/source data authorship is listed in the following database record: biostudies:S-SCDT-10_1038-S44319-026-00692-w.

Disclosure and competing interests statement

The authors declare no competing interests.

Expanded View Figures

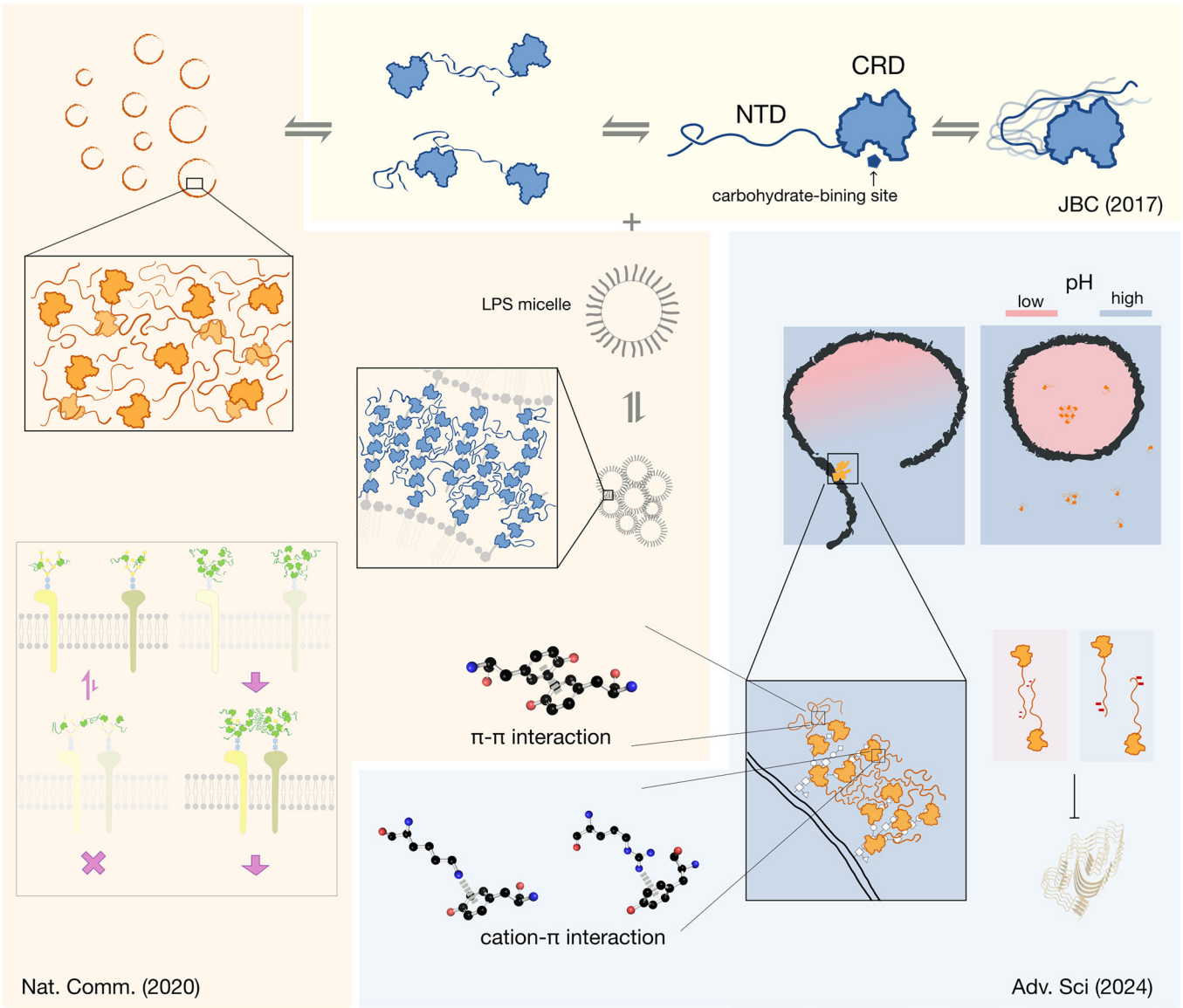

Figure EV1. Summary of previous studies on galectin-3 self-association.

Background shading groups panels by publication: yellow: JBC (Lin et al, 2017); peach: Nat. Commun. (Chiu et al, 2020); blue: Adv. Sci. (Sun et al, 2024). Galectin-3's intrinsically disordered N-terminal domain (NTD) forms transient intra- and intermolecular contacts with the non-carbohydrate-binding face of its carbohydrate-recognition domain (CRD; the NTD-binding face) and also self-associates (yellow). These interactions drive phase separation (PS) and enable galectin-3-mediated agglutination, assessed with lipopolysaccharide (LPS) micelles. Agglutination is supported by π-π interactions among aromatic residues within the NTD (peach) and by cation-π interactions between these aromatics and conserved, positively charged residues on the NTD-binding face. Two conserved acidic residues in the NTD modulate self-association in a pH-dependent manner (blue).

Appendix

for

Evolution of intrinsically disordered regions in vertebrate galectins for phase separation

Yu-Hao Lin, Yu-Chen Chen, Yung-Chen Sun, and Jie-rong Huang*

*Correspondence author: Jie-rong Huang

Email: jierongh@nycu.edu.tw

Table of contents

Supplementary Methods

Protein expression and purification

Fusion proteins (galectin variants and His_6-SUMO tags) were purified using nickel-charged immobilized metal-ion affinity chromatography (IMAC) columns (Qiagen). Imidazole was removed using a PD-10 column (Cytiva). Subsequently, His_6-$Ulp1^{403–621}$ protease was added to the protein solution at a concentration of 5 µg/ml for 1 h at 4 °C to cleave the His_6-SUMO tag from the galectin-3 variants. After enzyme digestion, the solution was injected into a nickel-charged IMAC column once more to separate the cleaved components and the flow-through containing the protein of interest was collected. The collected protein was loaded onto a HiLoad Superdex 75 pg gel-filtration column (Cytiva) with an FPLC system or a PD-10 column to exchange the appropriate buffer. Samples were flash-frozen in liquid nitrogen and stored at −80 °C before use.

NMR data collection and analysis

^{1}H-^{15}N HSQC spectra were recorded using the standard pulse sequence with WATERGATE solvent suppression (1, 2). The ^{15}N dimension was sampled with 128 increments and zero-filled to 1024 points in NMRPipe prior to Fourier transformation; the ^{1}H dimension was acquired with 2048 points. Chemical shifts were assigned using standard HNCA, HN(CO)CA, HNCO, HN(CA)CO, CBCA(CO)NH, and HNCACB experiments acquired with non-uniform sampling (25%) (3, 4). Spin relaxation rate experiments were performed using standard pulse sequences (1, 2, 5). ^{15}N R_2 and R_1 rate constants were determined using delay times of 17, 34, 51, 68, 85, and 102 ms, and 100, 200, 300, 600, 800, and 1000 ms, respectively. Peak intensities were fitted to an exponential decay relative to the delay times with a Monte Carlo procedure to estimate fitting errors. All dynamics data were collected in an interleaved manner with an interscan delay of 3 s. All NMR data were recorded on a Bruker AVIII 850 MHz spectrometer with a cryogenic probe at 303 K unless otherwise stated.

Data were processed using NMRPipe (6) and analyzed with SPARKY (7). Peak intensities and errors were determined using the non-linear line-shape analysis (nlinLS) function in NMRPipe based on the noise of the spectra. Intensity ratios were normalized to the number of scans. The average chemical shift difference ($\Delta\delta^{HN}$) was calculated using

$$\Delta\delta^{\mathrm{HN}} = \sqrt{\frac{(\Delta\delta_{\mathrm{H}})^2 + \left(\frac{1}{5}\Delta\delta_{\mathrm{N}}\right)^2}{2}}$$

where $\Delta\delta_H$ and $\Delta\delta_N$ are the differences in chemical shift between two HSQC spectra for the amide proton and nitrogen, respectively.

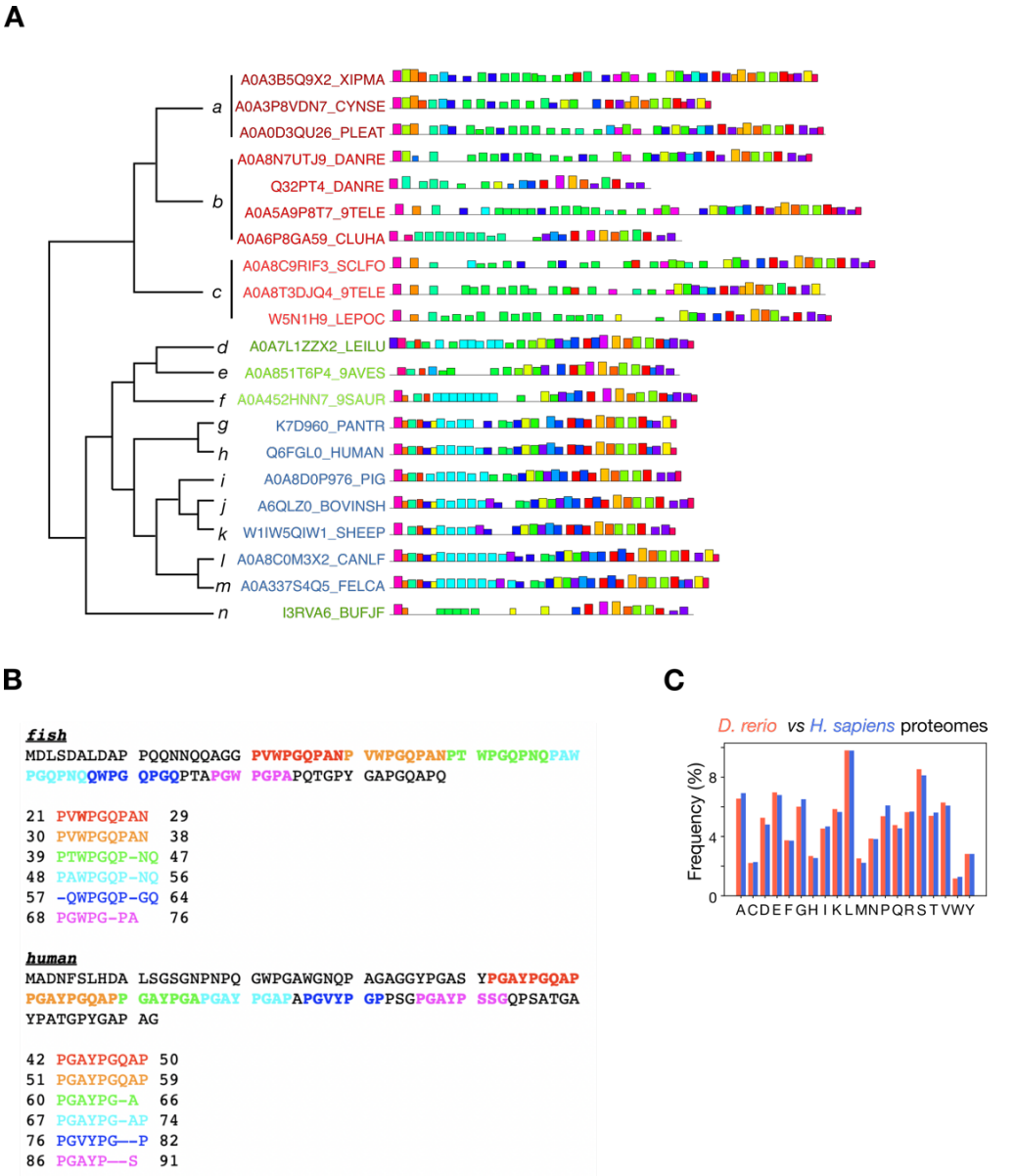

Appendix Figure S1. Sequence motifs of representative vertebrates and amino acid sequences of the studied zebrafish and human galectins. (A) Phylogenetic relationships and MEME motifs of selected galectin homologs across vertebrate clades. Branches labeled (*a*), (*b*), and (*c*) represent teleost fishes from *Euteleosteomorpha*, *Otomorpha* (within *Clupeocephala*), and *Osteoglossocephala*, respectively. Avian lineages are illustrated by (*d*) *Neognathae* and (*e*) *Paleognathae*, while (*f*) denotes a representative from *Sauria* (reptiles). Mammalian and amphibian sequences include chimpanzee (*g*), human (*h*), pig (*i*), bovine (*j*), sheep (*k*), dog (*l*), cat (*m*), and frog (*n*). Each sequence is indicated by its UniProt ID, and the colored blocks to the right represent distinct motifs identified with the MEME suite. The tree (left) is shown in simplified form to highlight phylogenetic relationships among selected taxa. (B) Sequences of zebrafish (UniProt ID: Q6TGN4) and human (P17931) IDR-tethered galectins; the repeated motifs in the intrinsically disordered regions are highlighted and aligned. (C) Amino-acid composition of *Danio rerio* and *Homo sapiens* proteomes.

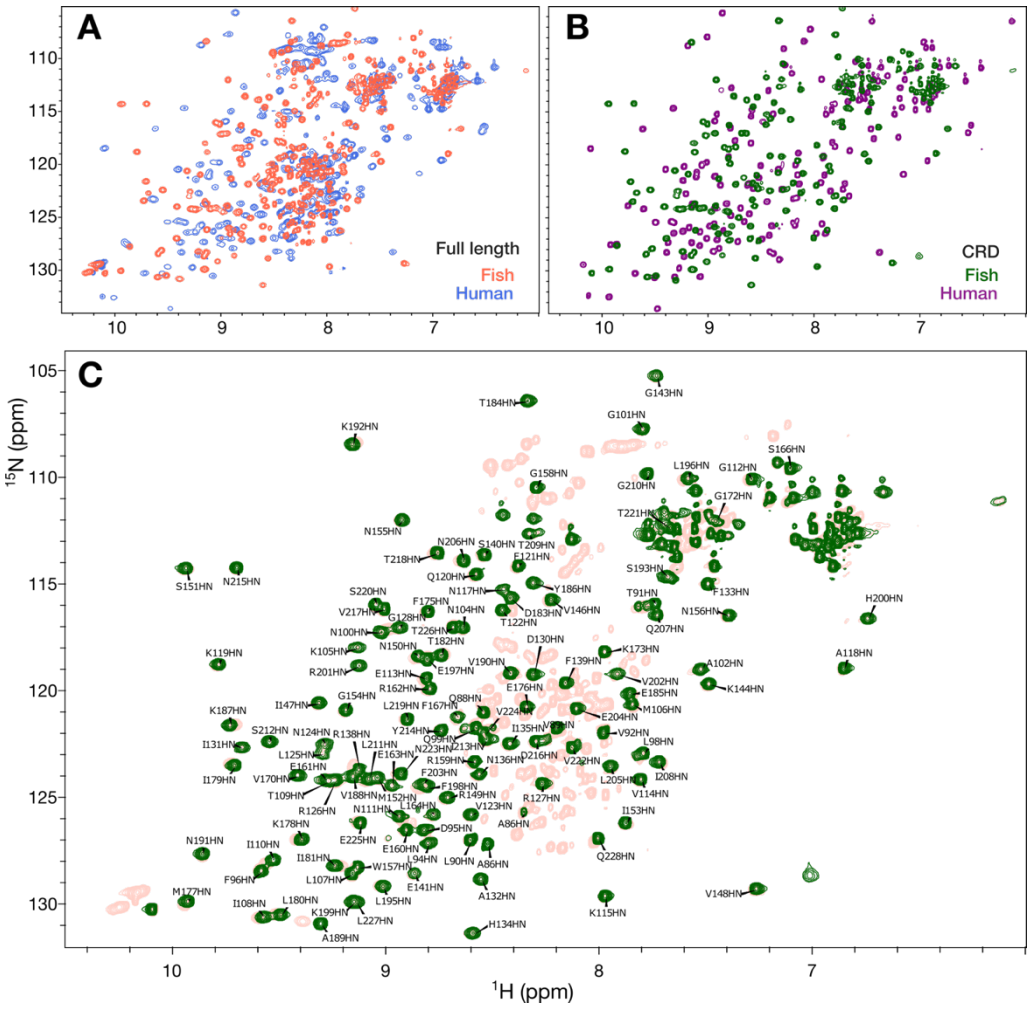

Appendix Figure S2. ^{1}H-^{15}N HSQC spectra of zebrafish and human IDR-tethered galectins. Overlaid ^{1}H-^{15}N HSQC spectra of (A) full-length and (B) carbohydrate-recognition domain (CRD)-only constructs of human and zebrafish IDR-tethered galectins. (C) Chemical shift assignments of the CRD of zebrafish IDR-tethered galectin (deposited in the BMRB (52443)) overlaid on the spectrum of the full-length protein (light red).

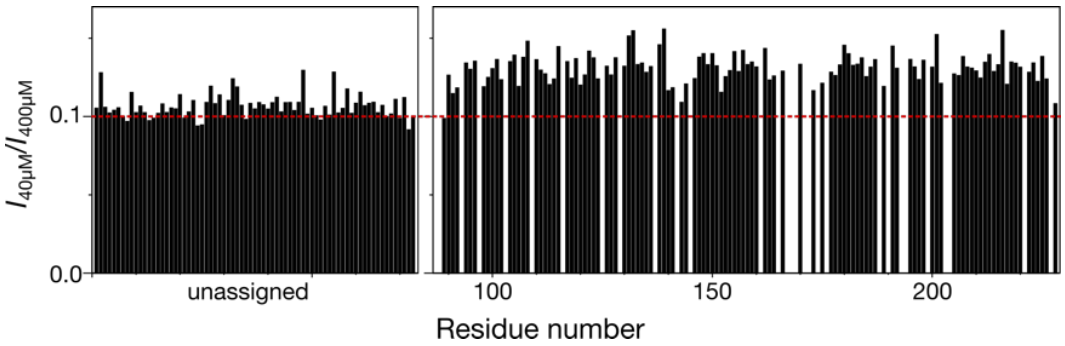

Appendix Figure S3. NMR peak intensity ratios between 40 μM and 400 μM zebrafish galectin samples. The red line shows the signal intensity ratio expected from the molar ratio (i.e., ignoring any intermolecular interactions).

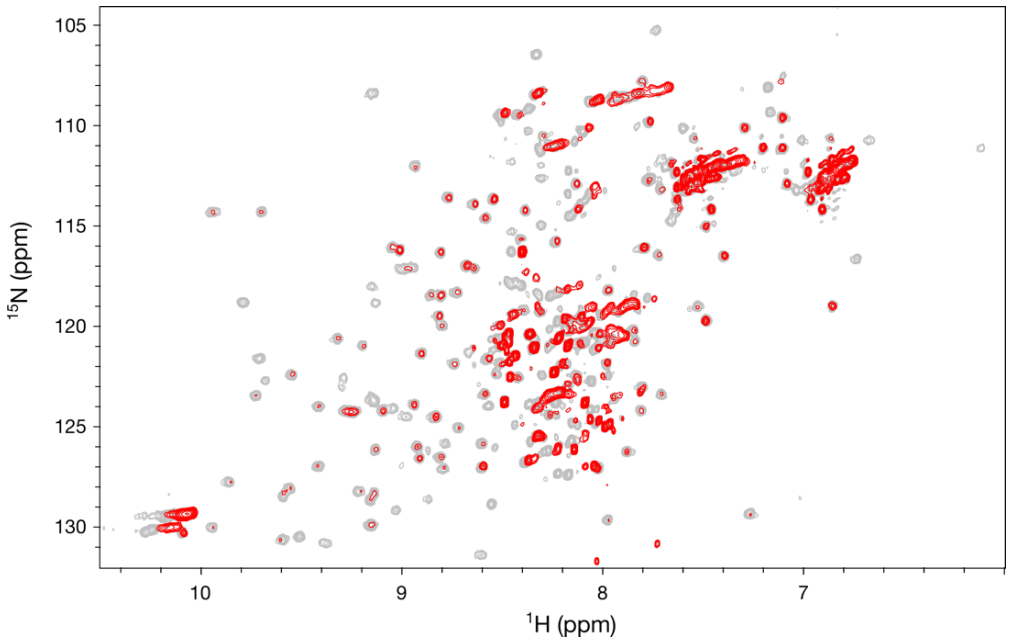

Appendix Figure S4. Overlaid ^{1}H-^{15}N HSQC spectrum of the IDR-augmented zebrafish galectin construct (zfGal^{aug}, red) and wild-type zfGal (gray), both at 40 µM, shown on the same intensity scale (same contour levels).

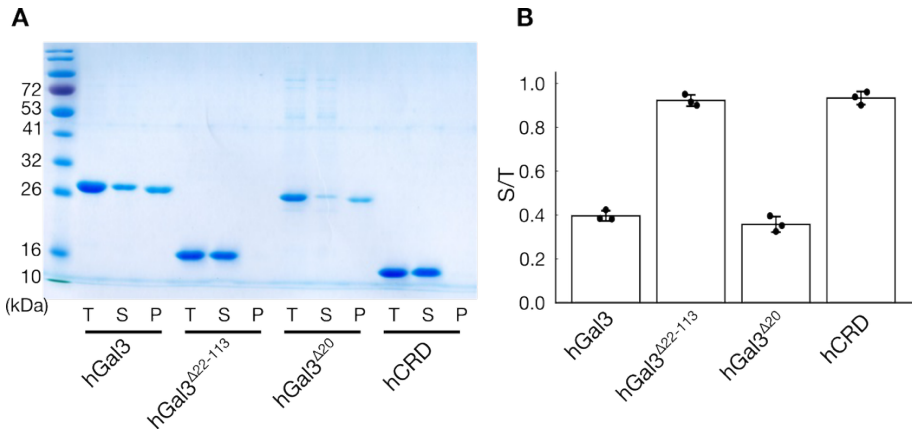

Appendix Figure S5. LPS-induced agglutination depends on the conserved galectin-3 N-terminus. Wild-type human galectin-3 (hGal3) is compared with two N-terminal variants: hGal3$^{\Delta 22–113}$, in which N-terminal domain (NTD) residues 22–113 are deleted, leaving only residues 1–21 N-terminal to the CRD, and hGal3$^{\Delta 20}$, in which NTD residues 1–20 are deleted, as well as the isolated carbohydrate-recognition domain (hCRD). (A) Coomassie-stained SDS–PAGE of the total reaction (T) and the corresponding supernatant (S) and pellet (P) fractions after incubation with LPS and centrifugation (conditions in Methods). (B) Protein in S and T quantified by Bradford assay (n = 3; mean ± s.d.).

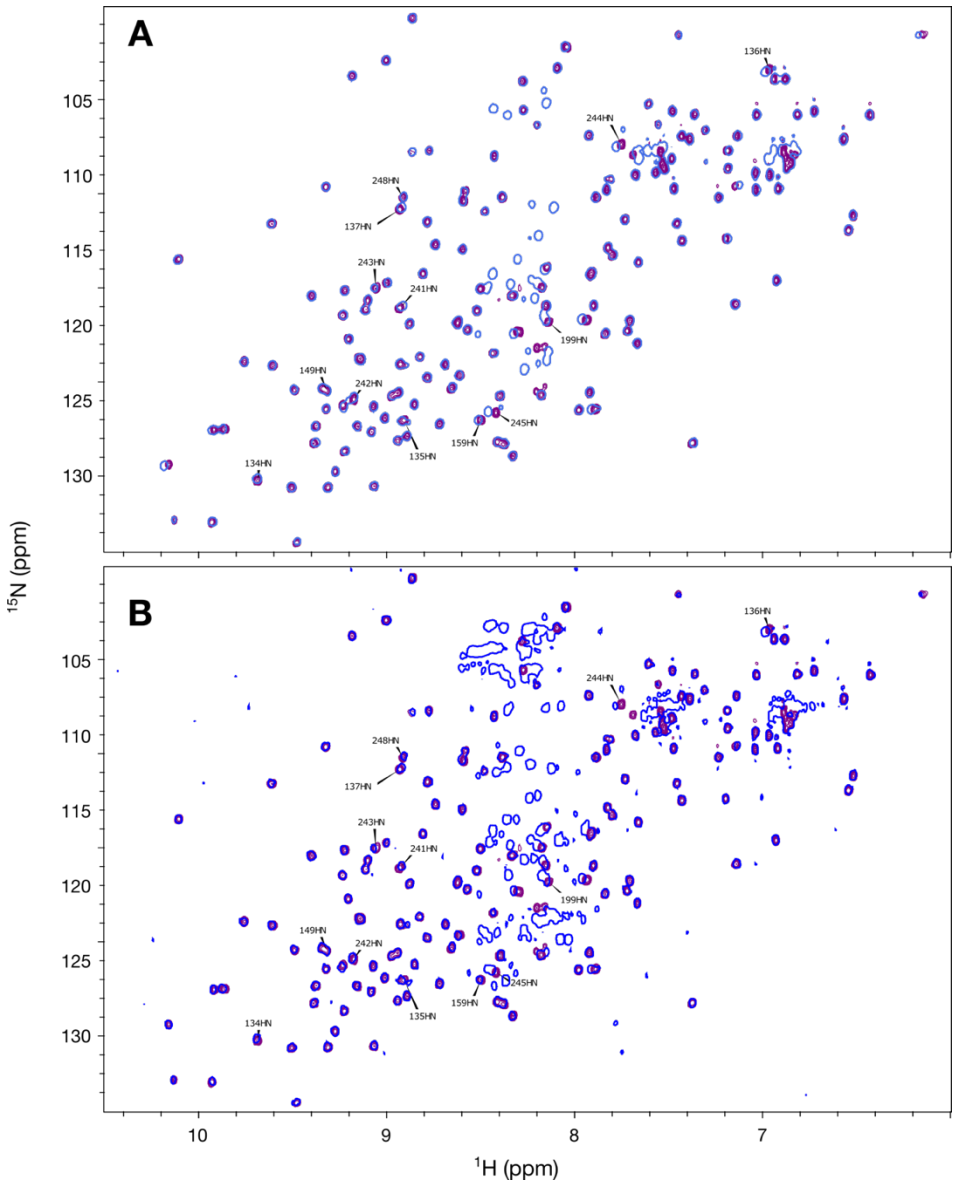

Appendix Figure S6. ^{1}H-^{15}N HSQC spectra of human galectin-3 variants (A) without residues 22–113 (hGal3$^{\Delta 21\text{-}113}$, blue contours) and (B) with all tryptophans and tyrosines in the intrinsically disordered region replaced by glycine (hGal3$^{WY/G}$, blue contours) overlaid onto the spectrum of the human CRD-only construct (purple). The peaks that shift the most between constructs are labeled (except those adjacent between the CRD and N-terminal IDRs).

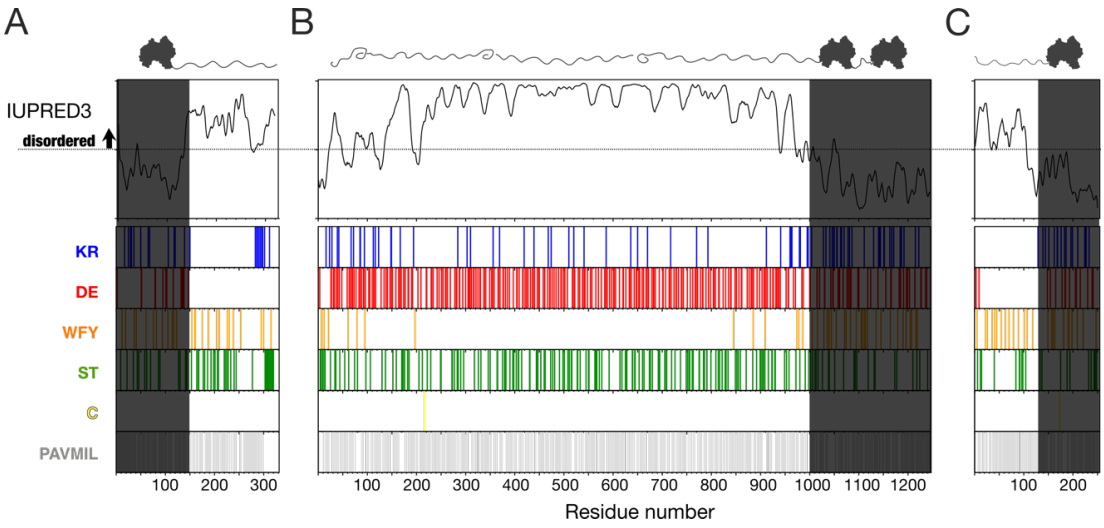

Appendix Figure S7. Comparison of carbohydrate recognition domains (CRDs) tethered to intrinsically disordered regions (IDRs) across three evolutionarily distant species. (A) A galectin-like protein from the plant *Rhodamnia argentea* (UniProt: A0A8B8QVV1), featuring an IDR appended to the C terminus with only positive charges. (B) A tandem-repeat galectin from *Caenorhabditis elegans* (UniProt: Q20684) with a long negative-charge dominant IDR. (C) Human galectin-3 (UniProt: P17931) is also shown for reference; its IDR contains only two negatively charged residues. Intrinsic disorder was predicted using IUPRED3. Colors indicate residues with different physicochemical properties (e.g., positively or negatively charged, aromatic).

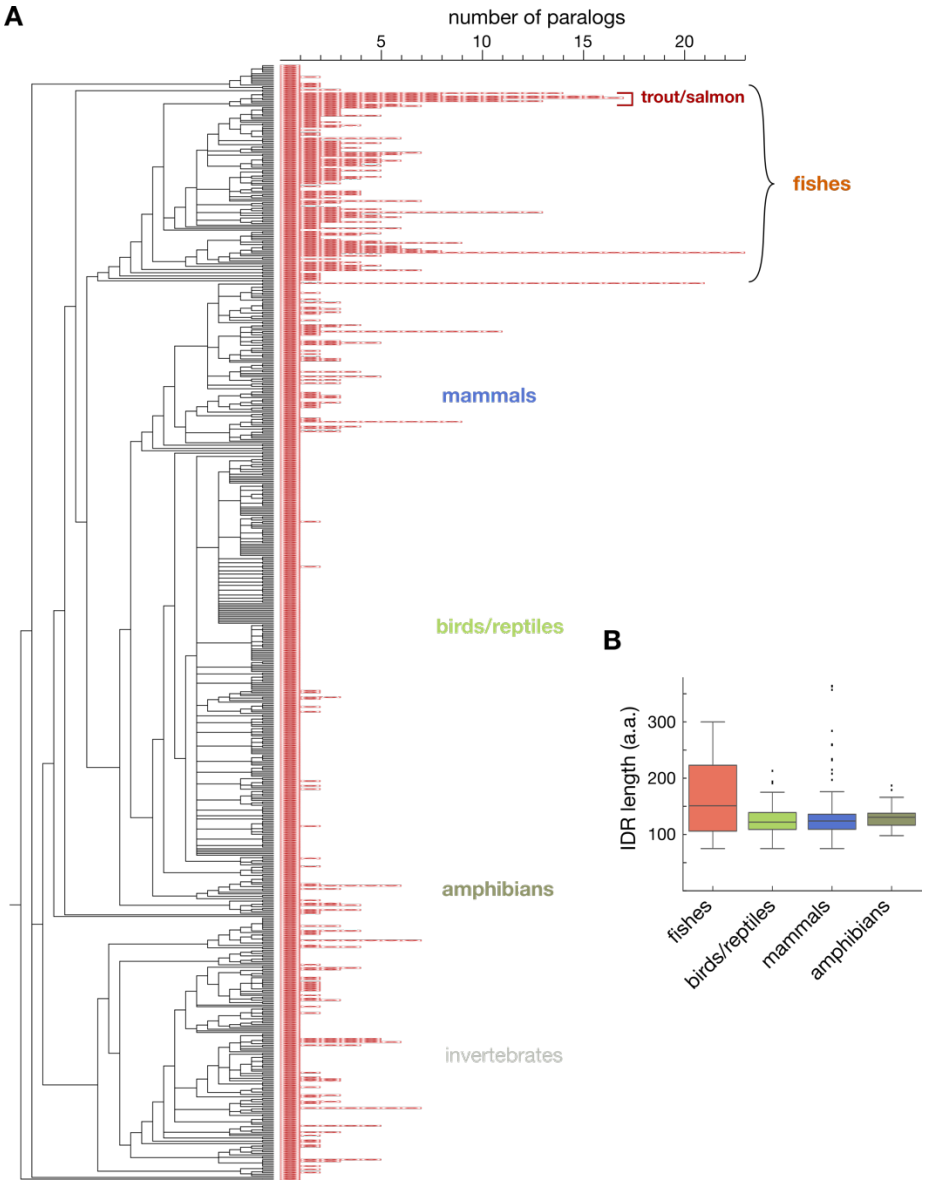

Appendix Figure S8. (A) Number of IDR-tethered galectin paralogs (red blocks) in different species. The phylogenetic tree is the same as shown in Dataset EV2. (B) The boxplot lengths distribution of different vertebrates.

Reference

1. M. Piotto, V. Saudek, V. Sklenar, Gradient-tailored excitation for single-quantum NMR spectroscopy of aqueous solutions. *J Biomol NMR* **2**, 661-665 (1992).
2. G. Bodenhausen, D. J. Ruben, Natural abundance N-15 NMR by enhanced heteronuclear spectroscopy. . *Chem. Phys. Letters* **69**, 185-189 (1980).
3. S. G. Hyberts, A. G. Milbradt, A. B. Wagner, H. Arthanari, G. Wagner, Application of iterative soft thresholding for fast reconstruction of NMR data non-uniformly sampled with multidimensional Poisson Gap scheduling. *J Biomol NMR* **52**, 315-327 (2012).
4. S. G. Hyberts, D. P. Frueh, H. Arthanari, G. Wagner, FM reconstruction of non-uniformly sampled protein NMR data at higher dimensions and optimization by distillation. *J Biomol NMR* **45**, 283-294 (2009).
5. N. A. Farrow *et al.*, Backbone dynamics of a free and phosphopeptide-complexed Src homology 2 domain studied by 15N NMR relaxation. *Biochemistry* **33**, 5984-6003 (1994).
6. F. Delaglio *et al.*, NMRPipe: a multidimensional spectral processing system based on UNIX pipes. *J Biomol NMR* **6**, 277-293 (1995).
7. T. D. Goddard, D. G. Kneller (2005) Sparky 3. San Francisco, University of California.